ORIGINAL RESEARCH ARTICLE

Liquid Structure and Thermophysical Properties of Ternary Ni-Fe-Co Alloys Explored by Molecular Dynamics Simulations and Electrostatic Levitation Experiments

J.F. ZHAO, H.P. WANG, P.F. ZOU, C.H. ZHENG, M.J. LIN, L. HU, and B. WEI

The structure, thermodynamic and dynamic properties of normal and metastable liquid $Ni_{2x}Fe_{50-x}Co_{50-x}$ alloys were systematically investigated by combining electrostatic levitation (ESL) experiments and molecular dynamics (MD) simulations. Their composition dependence and mutual interaction were explored in detail. The actual densities of liquid $Ni_{90}Fe_5Co_5$, $Ni_{80}Fe_{10}Co_{10}$, $Ni_{70}Fe_{15}Co_{15}$ and $Ni_{60}Fe_{20}Co_{20}$ alloys were measured by ESL experiments in a wide temperature range. The simulated densities of these liquid alloys are in good agreement with the corresponding experimental data. The thermodynamic properties show that all these alloys exhibit a negative excess volume and mixing enthalpy. Meanwhile, their pair distribution functions indicate that Fe and Co atoms easily bond with Ni atoms and have a similar characteristic to each other if compared with Ni atoms. Furthermore, the structure factors validate that there exist icosahedral short-range and medium-range orders of Ni-Ni, Fe-Fe, Fe-Co and Co-Co bonds in these liquid alloys. Additionally, the solute diffusion properties reveal that the correlation between dynamic behavior and alloy composition is determined by the diffusion of Fe and Ni atoms.

https://doi.org/10.1007/s11661-021-06185-w

I. INTRODUCTION

THE liquid structure and thermophysical properties of multicomponent liquid alloys, especially for undercooled liquids, are important fundamental issues in the numerical simulation and theoretical modeling for describing liquid physics and phase transformation,[1–3] which have been paid great attention in the fields of condensed matter physics, materials physics, atomic and molecular physics. There is a close relationship between the liquid structure and thermophysical properties. The liquid structure reveals the characteristics of atom distribution, atom packing degree, and neighbor distance, *etc.*[2,4] Meanwhile, the thermophysical properties are helpful to understand the heat transfer, mass transport and convection during the liquid/solid phase transition.[4–6] The thermophysical properties are the macro representation of atomic distribution, therefore, it is necessary to study the constitutive relationship between those properties.

As a fundamental thermophysical property, the density of liquid alloys plays a crucial role, since the measurement of other thermophysical properties, such as viscosity and surface tension, requires the accurate density data.[7] However, the measured densities of liquid alloys are limited in a narrow temperature range with poor accuracy by traditional measurement methods, because of the high chemical reactivity which causes the reaction between the high temperature metallic melts and the test apparatus. In recent decades, fortunately, the containerless techniques have been developed to measure the thermophysical properties of high temperature metallic melts, especially under the undercooled states. There are two main containerless techniques to measure the density of high temperature metallic melts: electromagnetic levitation (EML) and electrostatic levitation (ESL). Compared to EML, the sample in ESL has higher stability and less deviation from spherical shape which allows higher measurement accuracy of volume, *i.e.*, density. Therefore, the ESL is an effective method to obtain the density of metallic melts.[2,6–9] This provides a powerful approach to study the high temperature alloys.

As a typical high temperature alloy, the Ni-Fe-Co based steels with exceptional tensile strength and ductility have been widely applied in automobile, aerospace

J.F. ZHAO, H.P. WANG, P.F. ZOU, C.H. ZHENG, M.J. LIN, L. HU, B. WEI are with School of Physical Science and Technology, Northwestern Polytechnical University, Xi'an 710072, China. Contact e-mail: hpwang@nwpu.edu.cn

Manuscript submitted September 3, 2020; accepted February 1, 2021.

Article published online March 16, 2021

and land-based gas turbine engines. In the past decade, many researchers have reported the densities of multi-component metallic melts, such as Fe-Co-Cu alloys,[10] Fe-Ni-Cu alloys,[11] Fe-Cr-Ni alloys,[12] Inconel 718 alloy[13] and so on,[14–16] where the accurate density of metallic melts can help achieve alloy design and preparation. However, the researches of Ni-Fe-Co system are still limited to binary alloys. There is a lack of densities of Ni-Fe-Co ternary alloys for optimizing alloy composition and guiding industrial production. Brillo *et al.*[17] measured the density of Fe_xCo_{1-x} alloys by using EML technique. Furthermore, Lee *et al.*[6] reported the density of liquid Fe-Co binary alloy *via* ESL and indicated that the Fe-Co alloy almost like an ideal solution. Paradis *et al.*[18] measured the densities of Fe-Ni alloys by ESL containerless technique. Kobatake *et al.*[19] systematically investigated the densities of liquid Fe-Ni alloys over a wide temperature range *via* EML method, and discussed the evolution of density as a function of alloy composition. Watanabe *et al.*[20] accurately determined the densities of Fe-Ni alloys in a wide temperature range by combining the EML and static magnetic field, and compared the results of themselves with Paradis *et al.*[18] and Kobatake *et al.*[19] which indicates their data agree well with those obtained by Paradis *et al.*[18]

For Ni-Fe-Co alloys, as the complicated solid phase transition occurs at high temperature, the stable levitation of solid sample will be broken before the melting during the ESL experiments. When the levitated solid sample was melted, the mass loss caused by evaporation can't be neglected for liquid Ni-Fe-Co alloys due to the high vapor pressure of pure elements (iron, cobalt and nickel). The mass loss will further increase, especially when the levitated liquid sample has undergone at least three melting-solidification cycles. Therefore, the mass of sample should be carefully considered as a function of time and temperature during melting-solidification. However, the evaluation of mass loss during the ESL experiments is a hard task, due to complicated thermodynamic and dynamic properties of Ni-Fe-Co alloys. Moreover, almost all evaporating materials will move to the vertical electrodes in the electrostatic field, leading to the tip discharge which will cause the failure of experiments. This brings great difficulties to determine the density data of Ni-Fe-Co alloys.

Because of the difficulty of the ESL experiments, the systematically experimental research of Ni-Fe-Co alloys is limited. In order to systematically investigate the thermophysical properties of Ni-Fe-Co alloys and the microscopic mechanism of thermophysical properties, the molecular dynamics (MD) simulation is a proven tool. The liquid structure and dynamic properties can be determined according to the atomic arrangement during the MD simulation. The structures of atomic scale determine the thermophysical properties of liquid alloys and further affect the solidification behavior.[4,21–23] On the other hand, the dynamic properties, especially under the undercooled state, play an important role in understanding the solidification process.[24–26] Therefore, a comprehensive analysis of the relationship between the structural, thermodynamic and dynamic properties of liquid alloys is imperative. Although some researches on the relationship between the structure and dynamics or thermodynamic have been reported,[27–30] there is still a lack of comprehensive analysis of structural, thermodynamic and dynamic properties. In order to investigate the constitutive relationship between the structural, thermodynamic and dynamic properties, it is necessary to systematically analyze the relationship between those three properties with compositions.

Our goal is to solve the following three questions. Is it possible to accurately measure the density of liquid Ni-Fe-Co using ESL technique? What is the microscopic mechanism of the thermodynamic properties change with compositions? What is the relationship among the structure, thermodynamic and dynamic properties? To this end, the structural, thermodynamic and dynamic properties of liquid Ni-Fe-Co alloys were systematically investigated by combing the ESL experiments and MD simulation. Figure 1(a) presents the schematic of this work. We will use density as the main body to systematically investigate the constitutive relationship between the structure, thermodynamic and dynamic properties by establishing the connection between $g(r)$, $S(q)$, D and ΔH_{mix}. Figure 1(b) shows the Ni-Fe-Co ternary phase diagram[31] and the alloy compositions $Ni_{2x}Fe_{50-x}Co_{50-x}$ (x = 5, 10, 15, …, 50) of this work. The accurate densities, in a wide temperature range, of liquid $Ni_{90}Fe_5Co_5$, $Ni_{80}Fe_{10}Co_{10}$, $Ni_{70}Fe_{15}Co_{15}$ and $Ni_{60}Fe_{20}Co_{20}$ alloys were obtained *via* ESL experiments combined with the correction of mass evaporation. Meanwhile, the thermodynamic properties of liquid $Ni_{2x}Fe_{50-x}Co_{50-x}$ alloys were studied by MD simulation. Further, the microscopic mechanism which determines the thermodynamic properties was analyzed according to the structural and dynamic properties. Moreover, the constitutive relationship between the structural, thermodynamic and dynamic properties was discussed based on the MD simulation, the corresponding physical parameters are shown in Figure 1(a).

II. EXPERIMENTS AND SIMULATIONS

A. *Alloys Preparation and Thermal Analysis*

The $Ni_{2x}Fe_{50-x}Co_{50-x}$ (x = 5, 10, 15, …, 50) alloys were prepared from pure Ni (99.995 pct), pure Fe (99.99 pct) and pure Co (99.999 pct) in an arc melting furnace. The pure Ar atmosphere and titanium oxygen getter were used to prevent the oxidation of master alloys. To obtain a uniform composition of master alloy with about 500 mg, the melting process was repeated four times. The small samples with 35 mg were cut from the master alloys and used for further experiments.

The thermal analysis experiments were carried out using the Netzsch DSC 404C differential scanning calorimeter. The measurement uncertainty of temperature is ± 1 K in the temperature range of 300 K to 1800 K. Before the DSC experiment, the small alloy specimen was placed in an Al_2O_3 crucible. The chamber was evacuated by a mechanical vacuum pump and backfilled argon gas to prevent oxidation. The alloy specimen was heated with a heating rate of 10 K/min under an argon

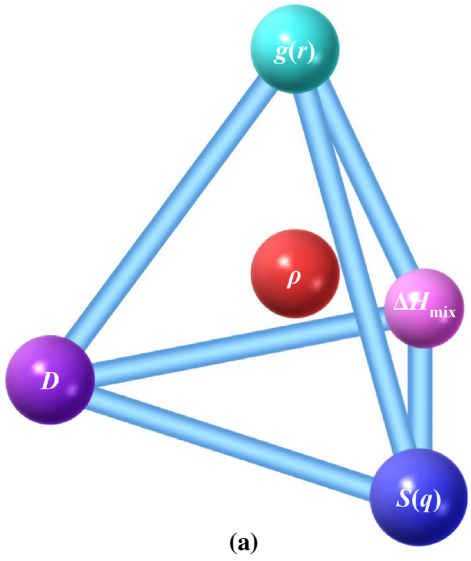

(a)

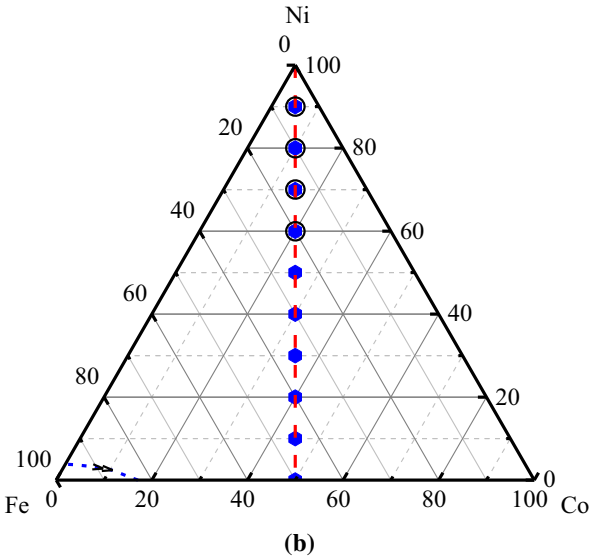

(b)

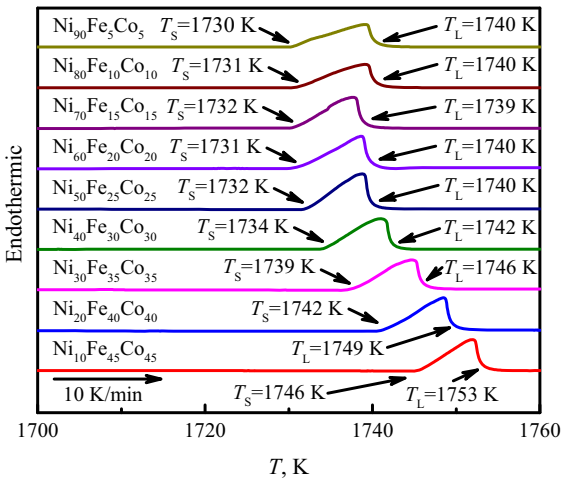

(c)

◀Fig. 1—The starting point of this work: (*a*) schematic of correlated physical parameters; (*b*) selection compositions of ternary Ni-Fe-Co alloy; (*c*) DSC thermal analysis curves of different alloys.

atmosphere with a flow rate of 60 mL/min. The DSC heating curves of $Ni_{2x}Fe_{50-x}Co_{50-x}$ alloys in the temperature range of 1700 K to 1760 K are shown in Figure 1(c). The solidus temperature T_S and liquidus temperature T_L of a series of alloys determined by DSC heating curves are listed in Figure 1(c) and Table I. Obviously, the T_S and T_L decrease with the increase of Ni content.

B. *Density Measurement by Electrostatic Levitation Technique*

The experiments of density measurement were executed by ESL system, the more information about ESL system was described in References 8 and 32. The small sample was preheated at 1300 K in a ~10^{-5} Pa vacuum chamber. The sample was levitated and stabilized under the coupling effect of the two vertical electrodes with four side electrodes. When the sample was stably levitated, it was heated and melted using the SPI SP 300 fiber laser with $\lambda = 1070$ nm. The temperature of the levitated liquid sample was measured using the SENSORTHERM GMBH METIS M3 22 two-color ratio pyrometer which works in the range of 873 K to 2573 K and operates at $\lambda = 1.4$ μm and $\lambda = 1.64$ μm. The emissivity ratio was calibrated by matching the melting plateau with DSC melt curve. In the ESL experiments, the melting plateau of temperature curve corresponds to the solidus temperature T_S of alloys. When the laser was turned off, the superheated liquid sample would cool off by thermal radiation. At the same time, the profile of liquid alloy was recorded by a CMOS camera with an image size of 704 × 700 pixels at a frequency of 100 Hz under the ultraviolet background light until the recalescence occurred, the more detailed information about the measurement was described in Reference 33. In order to accurately measure the density of alloys, the sample undergoes at last three times melting-solidification processes in an ESL experiment.

After the ESL experiment, the images were digitized by gray scale and analyzed by edge detection algorithm. The edge curve $R(\varphi)$ of liquid alloy, where R and φ are the radius and azimuthal angle, was fitted by the Legendre polynomials of 6 orders. The equilibrium shape of liquid alloy is rotationally symmetric in the vertical direction, hence, the volume of liquid alloy can be calculated by using the following integral

$$V(T) = \frac{2}{3}\pi q^3 \int_0^{\pi} R^3(\varphi, T)\sin(\varphi)\mathrm{d}\varphi \qquad [1]$$

where q is the scaling factor that is determined by using a standard steel ball whose mass and density are known and T is the temperature of the liquid alloy.

As the vapor pressures of iron, cobalt and nickel are considerably high, the mass loss caused by evaporation of liquid sample can not be neglected during ESL experiments. The mass loss will be further increased, especially when the sample has undergone at least three times melting-solidification processes. Therefore, the mass of sample becomes a function of time and temperature during the melting cycle. According to the Lee and Matson's prediction function of mass loss,[34] the total mass loss during the melting-solidification cycle can be described:

$$m_t = \sum_{i=1}^{n} \left[\int_{t_0}^{t} \frac{\alpha_i A_i a_i (P_{\mathrm{v},i} - P_{\mathrm{ref}})}{\sqrt{2\pi M_i R T}} \mathrm{d}t^* \right] \quad [2]$$

where, for component i, α_i is the degree of actual deviation from the ideal mass evaporation, A_i the effective surface area, a_i the activity, $P_{\mathrm{v},i}$ the vapor pressure, P_{ref} the reference pressure, M_i the molecular mass, T the temperature, and R is the gas constant.

The mass of sample can be determined by the difference of the initial mass m_0 and the lost mass m_t, *i.e.* $m(t) = m_0 - m_t$. According to the temperature *vs.* time curve measured by the pyrometer, the mass as a function of time $m(t)$ can be transformed to the mass as a function of temperature $m(T)$. Then the density of liquid alloy is expressed by

$$\rho(T) = \frac{m(T)}{V(T)} \quad [3]$$

C. *Molecular Dynamics Simulation of Liquid State*

The vapor pressures of iron and cobalt are higher than that of nickel, therefore, the ESL experiments of the compositions with low Ni content are very difficult. To systematically investigate the density and other properties of liquid Ni-Fe-Co ternary alloys, the molecular dynamics simulation was performed by the second nearest-neighbor modified embedded-atom method (2NN MEAM). The 2NN MEAM potential can accurately describe a wide range of elements with different phases (bcc, fcc, hcp, diamond, glass, liquid and gases) and be used in molecular dynamics and Monte Carlo simulations of unary, binary, ternary and multicomponent metallic systems.

In the 2NN MEAM potential,[35–38] the formulation of total energy of system can be described by

$$E_{\mathrm{tot}} = \sum_i \left[F(\rho_i) + \frac{1}{2} \sum_{j(j \neq i)} S_{ij} \phi_{ij}(R_{ij}) \right] \quad [4]$$

where F is the embedding function for an atom i embedded in a background electron density ρ_i, S_{ij} and ϕ_{ij} are the screening function and pair interaction between atoms i and j with a distance R_{ij}, respectively. The embedding function is expressed by

$$F(\rho_i) = \begin{cases} AE_c \frac{\rho_i}{\rho^0} \left(\ln \frac{\rho_i}{\rho^0} \right) & \rho_i \geq 0 \\ -AE_c \frac{\rho_i}{\rho^0} & \rho_i < 0 \end{cases} \quad [5]$$

where A is a variable parameter, E_c the cohesive energy, and ρ^0 is the background electron density of the reference structure. The pair interaction is given by

$$\phi(R) = \frac{2}{Z^0} \{ E^u(R) - F[\rho^0(R)] \} \quad [6]$$

where E^u is the universal function for a uniform expansion or contraction in the reference structure and Z^0 is the nearest neighbor coordination number of the reference structure. The more detailed information of above parameters was described in References 36 and 39.

Very recently, Wang *et al.*[40] reported the 2NN MEAM potential parameters of Ni-Fe-Co ternary alloy for simulating the thermal expansion; Farkas *et al.*[41] presented an embedded-atom method (EAM) potential of Fe-Co-Ni-Cr-Cu five-component high-entropy alloy to predict the stable phase of solid state. Compared with the 2NN MEAM potential, the simulation results of liquid Ni-Fe-Co using the EAM potential is disappointing, maybe because this EAM potential was developed to investigate the properties of solid state. On the contrary, the calculated densities of Ni-Fe-Co alloys using 2NN MEAM potential agree well with the experimental data which are shown in the following chapters of this work. Therefore, the 2NN MEAM potential is a better choice to investigate the thermophysical properties of liquid Ni-Fe-Co alloys. We used this potential to investigate the properties of liquid Ni-Fe-Co ternary alloys. The simulation was performed by the LAMMPS that is a classical molecular dynamics code.[42] In order to consider the atoms of the second nearest-neighbor in the simulations, the radial cutoff distance is defined as 5.0 Å. The 16,000 atoms were randomly distributed on the bcc supercell lattice with a superlattice size of 20 × 20 × 20 unit cells, and the ratio of three elements were set according to the composition of alloys. The supercell was calculated under isothermal-isobaric ensemble and periodic boundary condition. The time step was set to 1 fs, the pressure was defined as 1 bar, and the temperature was regulated every 5 time steps. The temperature decreased from 3000 K to 1100 K with a 100 K interval, and the cooling rate is 10^{12} K/s. The simulation system was relaxed 400 ps at every equilibrium temperature and the last 200 ps was used to calculate the thermophysical and structure properties of liquid alloys.

D. *Liquid State Structure*

The pair distribution function and static structure factor are classical methods to analyze the atom structure of liquid or amorphous alloys. The Faber–Ziman partial pair distribution function,[43] $g_{ij}(r)$, describes the probability density of j atoms appear with distance r from i atoms. The formulation of partial pair distribution function is defined by[27]

Table I. Measured and Calculated Density of Liquid $Ni_{2x}Fe_{50-x}Co_{50-x}$ alloys

Compositions	T_S (K)	T_L (K)	ρ_0 (g·cm^{-3})	$\partial\rho_L/\partial T$ (10^{-4} g·cm^{-3}·K^{-1})	β_L (10^{-4} K^{-1})	ρ (1700 K) (g·cm^{-3})	ρ_{N1} (10^{-2} atoms·Å^{-3})	Temperature Range (K)	Note
Ni	1728	1728	7.714	− 7.428	9.630	7.734	8.185	1400–3000	MD
$Ni_{90}Fe_5Co_5$	1730	1740	7.737	− 7.156	9.250	7.765	8.167	1400–3000	MD
			7.868	− 6.625	8.420	7.896	–	1560–1840	Exp.
$Ni_{80}Fe_{10}Co_{10}$	1731	1740	7.766	− 6.830	8.795	7.793	8.175	1400–3000	MD
			7.813	− 6.928	8.868	7.841	–	1550–1780	Exp.
$Ni_{70}Fe_{15}Co_{15}$	1732	1739	7.780	− 6.563	8.435	7.806	8.142	1400–3000	MD
			7.761	− 6.827	8.796	7.788	–	1450–1820	Exp.
$Ni_{60}Fe_{20}Co_{20}$	1731	1740	7.776	− 6.297	8.098	7.801	8.134	1400–3000	MD
			7.690	− 6.645	8.641	7.717	–	1420–1800	Exp.
$Ni_{50}Fe_{25}Co_{25}$	1732	1740	7.756	− 6.062	7.816	7.780	8.058	1300–3000	MD
$Ni_{40}Fe_{30}Co_{30}$	1734	1742	7.720	− 5.853	7.582	7.745	8.004	1100–3000	MD
$Ni_{30}Fe_{35}Co_{35}$	1739	1746	7.669	− 5.666	7.389	7.695	7.929	1100–3000	MD
$Ni_{20}Fe_{40}Co_{40}$	1742	1749	7.607	− 5.522	7.260	7.634	7.869	1100–3000	MD
$Ni_{10}Fe_{45}Co_{45}$	1746	1753	7.533	− 5.432	7.211	7.562	7.774	1200–3000	MD
$Fe_{50}Co_{50}$	1751	1752	7.451	− 5.359	7.193	7.479	7.693	1200–3000	MD

$$g_{ij}(r) = \frac{V}{N_i N_j}\left\langle \sum_{i=1}^{N_i} \frac{n_{ij}(r,\Delta r)}{4\pi r^2 \Delta r} \right\rangle \quad [7]$$

where V is the volume of simulation system, N_i the number of type atomic i, n_{ij} the number of j atoms in the spherical shell with distance r from i atoms, and Δr is the thickness of spherical shell. The Faber–Ziman partial static structure factor,[43] $S_{ij}(q)$, can be deduced from partial pair distribution function $g_{ij}(r)$ by Fourier transformation.[44]

$$S_{ij}(q) = 1 + 4\pi\rho_N \int_0^\infty \left[g_{ij}(r) - 1\right] \frac{\sin qr}{qr} r^2 \mathrm{d}r \quad [8]$$

where ρ_N is the number density of atoms and q is the wave vector in the inverted space.

The Faber–Ziman partial static structure factors describe the short-range order about different types of atoms. Bhatia and Thornton[45] have given a new formalism about the partial static structure factor to investigate the topological and chemical short-range order of binary alloys.[44–47] The Bhatia–Thornton partial static structure factor can be expressed by Faber–Ziman partial static structure factor[44]:

$$S_{NN}(q) = x_i^2 S_{ii}(q) + x_j^2 S_{jj}(q) + 2x_i x_j S_{ij}(q) \quad [9]$$

$$S_{NC}(q) = x_i x_j\left\{x_i\left[S_{ii}(q) - S_{ij}(q)\right] - x_j\left[S_{jj}(q) - S_{ij}(q)\right]\right\} \quad [10]$$

$$S_{CC}(q) = x_i x_j\left\{1 + x_i x_j\left[S_{ii}(q) + S_{jj}(q) - 2S_{ij}(q)\right]\right\} \quad [11]$$

where x_i and x_j are the concentrations of type i atom and j atom, respectively.

The number-number partial static structure factor, $S_{NN}(q)$, describes the topological properties of system and ignores the difference of atomic types, *i.e.*, topological short-range order. The $S_{CC}(q)$ is the concentration-concentration partial static structure factor, and describes the order of different chemical atom types at atom sites. The $S_{NC}(q)$ represents the coupling of number and concentration of atoms. When the binary alloy can be regarded as an ideal solution, the $S_{CC}(q)$ is equal to a constant $x_i x_j$, the $S_{NC}(q) = 0$, and all information of system structure is reflected by $S_{NN}(q)$.

III. RESULTS AND DISCUSSION

A. *Thermophysical Properties of Liquid Ni-Fe-Co Alloys*

The densities of $Ni_{90}Fe_5Co_5$, $Ni_{80}Fe_{10}Co_{10}$, $Ni_{70}Fe_{15}Co_{15}$ and $Ni_{60}Fe_{20}Co_{20}$ alloys were accurately measured by ESL technique. In order to ensure the accuracy of experiments, the alloys undergone several melting-solidification cycles in one ESL experiment. Figure 2(a) shows the curve of temperature *vs.* time of $Ni_{70}Fe_{15}Co_{15}$ alloy, which has undergone four melting-solidification cycles. The maximum undercooling was achieved to be 300 K at the last melting-solidification cycle, and the minimum value of undercooling was 46 K at the second melting-solidification cycle. Except the second melting-solidification cycle is consistent with the third one, the superheating is increase with melting-solidification cycle in the ESL experiments and the maximum value of superheating is 88 K greater than the liquidus temperature 1739 K. Therefore, this suggests that the undercooling of alloys randomly distributes with the increase of melting-solidification cycle.

Due to the high vapor pressures of iron, cobalt and nickel elements, the mass evaporation can't be ignored in the experiments, especially when the sample has undergone four times melting-solidification cycles. The volume of liquid alloy at the same temperature will decrease with increasing the times of melting-solidification cycles. If the mass evaporation is ignored, the measured density of liquid alloy will increase with the times of melting-solidification processes, as indicated in

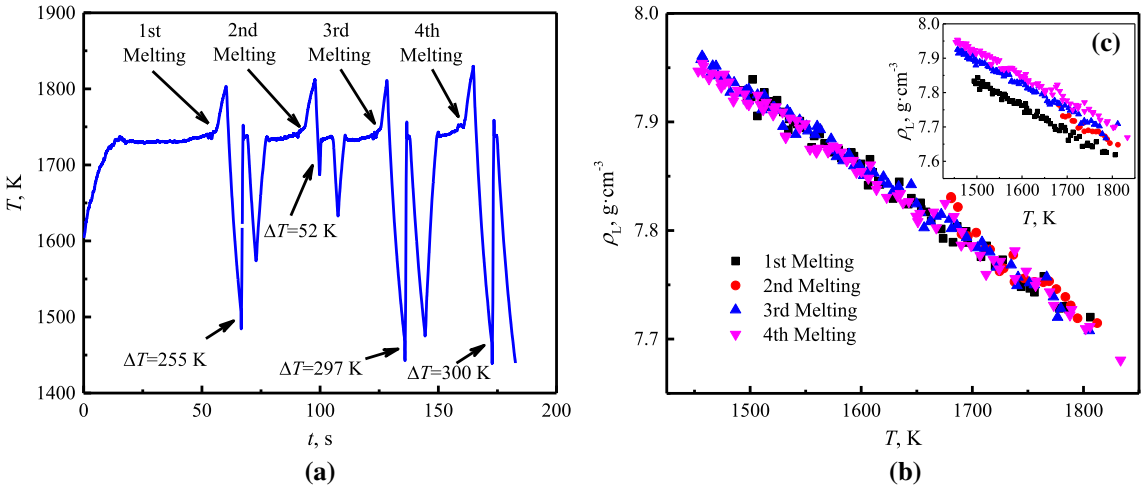

Fig. 2—The density measurement of liquid $Ni_{70}Fe_{15}Co_{15}$ alloy by electrostatic levitation technique: (*a*) heating and solidification of 4 cycles; (*b*) and (*c*) measured liquid density *vs*. temperature with and without the consideration of mass loss.

the inset in Figure 2(b). According to Eq. [2], the accurate mass of liquid alloy at every moment can be obtained in ESL experiment. Then, the density of liquid alloy after correction can be determined by bringing the mass into Eq. [3], as shown in Figure 2(b). The densities of different melting cycles are completely coincident after correction and linearly increase with the decreasing temperature. Usually the density of liquid alloys can be expressed by a linear function

$$\rho_L = \rho_0 + \frac{\partial \rho_L}{\partial T}(T - T_L) \qquad [12]$$

where ρ_0 is the density of liquid alloys at the liquidus temperature T_L and $\partial\rho_L/\partial T$ is the slope of the density changes with temperature. Since the $\partial\rho_L/\partial T$ is a very small value for the liquid alloys, the volume expansion coefficient β_L, the ratio of volume changes (δV) and volume (V) at unit temperature (δT), can be described by

$$\beta_L = \frac{1}{V}\frac{\partial V}{\partial T} = -\frac{1}{\rho_L}\frac{\partial \rho_L}{\partial T} \approx -\frac{\partial \rho_L/\partial T}{\rho_0} \qquad [13]$$

The accurate densities of $Ni_{90}Fe_5Co_5$, $Ni_{80}Fe_{10}Co_{10}$, $Ni_{70}Fe_{15}Co_{15}$ and $Ni_{60}Fe_{20}Co_{20}$ were measured by ESL experiments, as shown in Figure 3 and listed in Table I. According to Figure 3, it can be found that the maximum undercoolings of $Ni_{90}Fe_5Co_5$, $Ni_{80}Fe_{10}Co_{10}$, $Ni_{70}Fe_{15}Co_{15}$ and $Ni_{60}Fe_{20}Co_{20}$ alloys are 171 K, 189 K, 300 K and 312 K, respectively. The densities of alloys at liquidus temperature increase from 7.690 to 7.868 g·cm^{-3} with increasing content of Ni element, and the $\partial\rho_L/\partial T$ has a minimum value of -6.928×10^{-4} g·cm^{-3}·K^{-1} for $Ni_{80}Fe_{10}Co_{10}$ alloy. The volume expansion coefficient β_L of liquid alloys reaches the maximum value of 8.860×10^{-4} K^{-1}, when the content of Ni is 80 at. pct. In order to stably levitate the liquid alloys and reduce the composition deviation due to mass loss caused by evaporation, the superheating of liquid alloys was controlled at a lower level. According to the temperature range which is listed in Table I, the maximum superheating is 110 K of $Ni_{90}Fe_5Co_5$ alloy, and at the same time the total mass loss is also the largest.

The MD simulation was performed to calculate the properties of liquid $Ni_{2x}Fe_{50-x}Co_{50-x}$ ternary alloys so as to investigate the connection among these properties. Figure 3 and Table I present the densities of liquid alloys calculated by MD simulation, which show a well agreement with the experimental results. The density of pure Ni was measured by several researchers by using different methods.[20,48–50] Watanabe *et al.*[20] measured the density of liquid Ni in the range of 1490-1900 K by the electromagnetic levitation. Zou *et al.*[49] reported the experimental data of density of liquid Ni in a smaller temperature range *via* ESL. Furthermore, Brillo *et al.*[50] gave a credible average density value of Nickel ranging from 1553 to 1953 K, according to the several measurement data using the EML system. Figure 3(a) presents the experimental data and simulation results of liquid Ni at different temperature, and the calculated ρ_0 and $\partial\rho_L/\partial T$ can be determined as 7.714 g·cm^{-3} and − 7.467 g·cm^{-3}·K^{-1}. It can be seen that the simulated density is in good agreement with the experimental data of Brillo *et al.*[50] in the entire measurement temperature range, and smaller than the reported value of Watanabe *et al.*[20] and Zou *et al.*.[49] Although the simulated ρ_0 7.714 g·cm^{-3} is smaller than the experiment data 7.875 g·cm^{-3} and 7.89 g·cm^{-3} of Watanabe *et al.*[20] and Zou *et al.*,[49] the $\partial\rho_L/\partial T$ is similar to the result − 7.4 g·cm^{-3}·K^{-1} of Watanabe *et al.*.[20] The density of liquid $Fe_{50}Co_{50}$ alloy was measured by Brillo *et al.*[17] and Lee *et al.*[6] by using EML and ESL, respectively. Figure 3(b) shows that the results of simulation and experiments have an excellent consistency, and the difference of density at the liquidus temperature is smaller than 0.4 pct. The simulated and measured densities of $Ni_{90}Fe_5Co_5$, $Ni_{80}Fe_{10}Co_{10}$, $Ni_{70}Fe_{15}Co_{15}$ and $Ni_{60}Fe_{20}Co_{20}$ are shown in the insets of Figure 3(c) through (f). It can be seen that the simulation results are in accord with the experimental values, and the

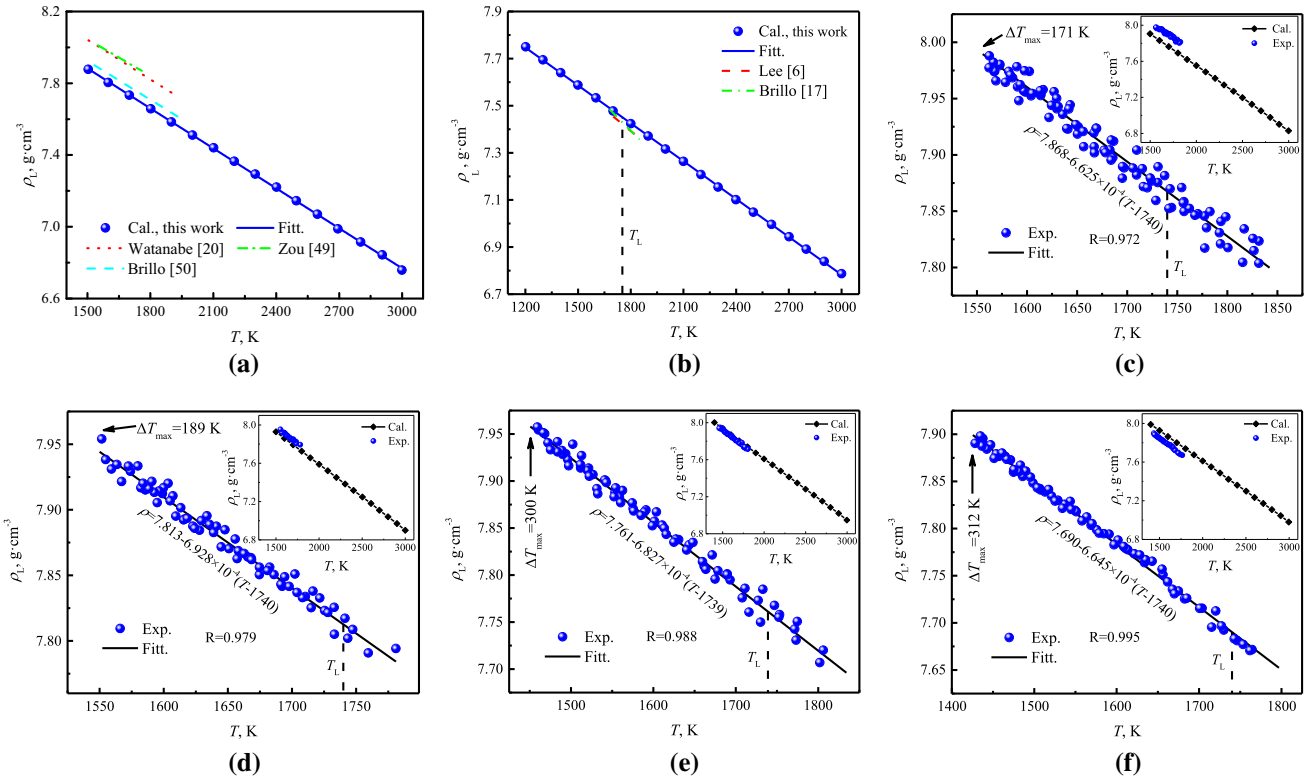

Fig. 3—Measured and calculated densities of liquid $Ni_{2x}Fe_{50-x}Co_{50-x}$ alloys *vs.* temperature: (*a*) Ni; (*b*) $Fe_{50}Co_{50}$ alloy; (*c*) $Ni_{90}Fe_5Co_5$ alloy; (*d*) $Ni_{80}Fe_{10}Co_{10}$ alloy; (*e*) $Ni_{70}Fe_{15}Co_{15}$ alloy; (*f*) $Ni_{60}Fe_{20}Co_{20}$ alloy.

maximum difference of ρ_0 between calculation and measurement is 1.67 pct for the liquid $Ni_{90}Fe_5Co_5$ alloy.

To systematically investigate the dependence of thermodynamic properties on different alloy compositions, the density, coefficient of volume expansion, excess volume and mixing enthalpy of liquid $Ni_{2x}Fe_{50-x}Co_{50-x}$ alloys *vs.* the content of Ni component were calculated and illustrated in Figure 4. Figure 4(a) presents the densities of liquid alloys at 1700 K where the sold line is the simulated data and the dash line represents the density of an ideal solution. It can be found that the deviation between the simulation and ideal solution results increases with the Ni content and then decreases when the content of Ni is larger than 50 pct. The coefficient of volume expansion raises from 7.193×10^{-4} K^{-1} to 9.630×10^{-4} K^{-1} as the Ni increases, as shown in Figure 4(b). The volume expansion of alloys is related to the atomic interaction. A large coefficient of volume expansion corresponds to a weak interaction between the atoms and implies a fast dynamic property. According to the Figure 4(b), the β_L slowly increases when the content of Ni is smaller than 40 at. pct and then rapidly increases. It suggests that the interactions of Ni-Fe and Ni-Co are similar with Fe-Co, and the interaction between Ni atoms plays a more important role in ternary Ni-Fe-Co alloys when the content of Ni is larger than 40 at. pct.

The deviation of density between the actual alloys and ideal solution can be described by the excessive volume ΔV_E and the ratio of ΔV_E and the molar volume of ideal solution V_0. The excessive volume is defined by

$$\Delta V_E = V_M - V_0 = \frac{x_1M_1 + x_2M_2}{\rho} - \left(\frac{x_1M_1}{\rho_1} + \frac{x_2M_2}{\rho_2}\right) \quad [14]$$

where V_M is the molar volume of actual alloys, for the component 1, x_1 molar fraction, M_1 atomic weight, ρ_1 density, and the subscript 1 and 2 represent Ni and $Fe_{50}Co_{50}$, respectively.

Based on Eq. [14], the ΔV_E of different compositions at 1700 K is calculated and illustrated in Figure 4(c). The black quadrilateral and blue hexagon in Figure 4(c) represent the excessive volume and $\Delta V_E/V_0$, respectively. It shows that the negative excessive volume occurs in $Ni_{2x}Fe_{50-x}Co_{50-x}$ alloys during the alloying. The ΔV_E first decreases to a minimum value when the Ni content reaches 50 at. pct, and then increases to zero again as the content of Ni increases. The similar relationship of the deviation degree $\Delta V_E/V_0$ with Ni content is also shown in Figure 4(c), and the maximum deviation degree is − 2.24 pct when the content of Ni is 50 at. pct.

In order to further investigate the extent to which the actual alloy deviates from the ideal solution during the alloying, the mixing enthalpy ΔH_{mix} of different compositions is also calculated, as shown in Figure 4(d). The mixing enthalpy $\Delta H_{mix} = H_M - H_0$, where H_M is the enthalpy of actual alloy and H_0 is calculated by using Neumann–Kopp's law. According to the Figure 4(d), it can be seen that the mixing enthalpy in $Ni_{2x}Fe_{50-x}Co_{50-x}$ alloys is negative and the shape of

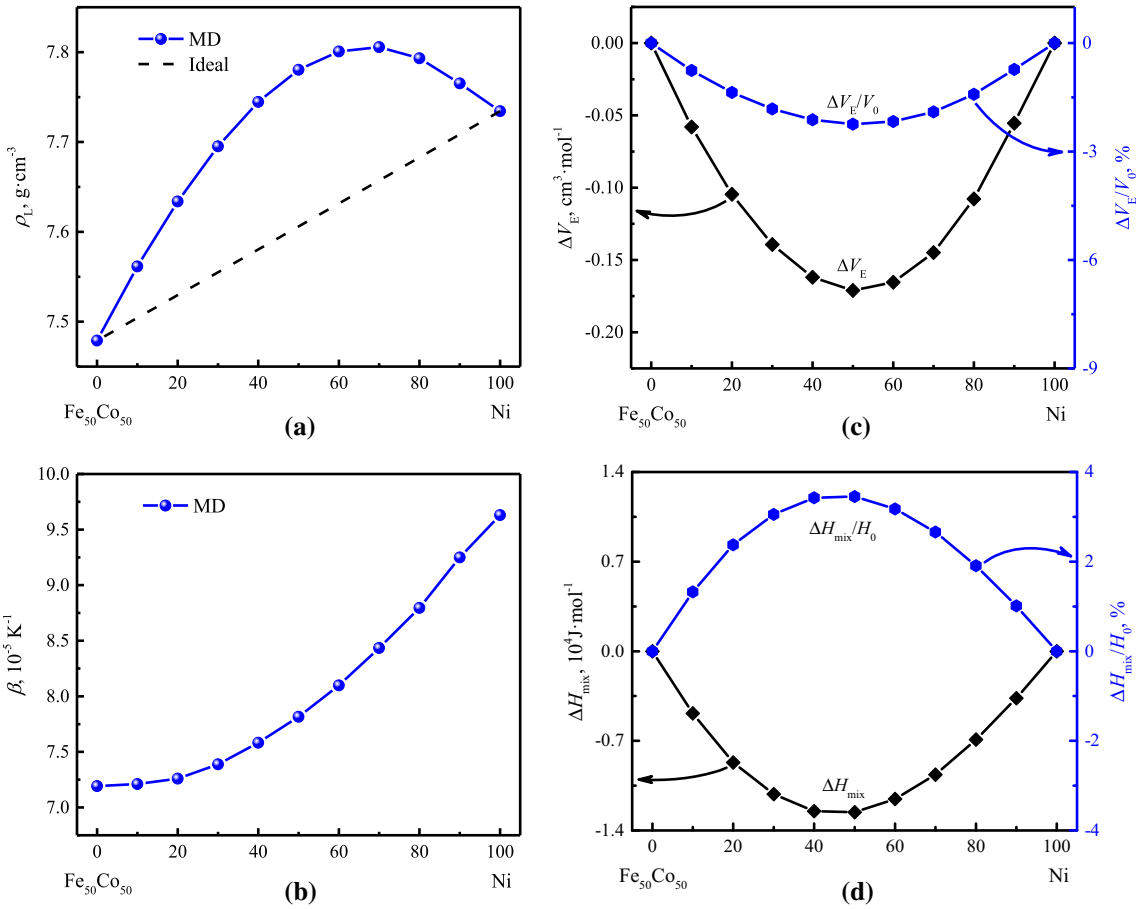

Fig. 4—The calculated thermodynamic properties of liquid $Ni_{2x}Fe_{50-x}Co_{50-x}$ alloys at 1700 K: (*a*) densities; (*b*) thermal expansion coefficient; (*c*) excess volume ΔV_E and $\Delta V_E/V_0$; (*d*) mixing enthalpy ΔH_{mix} and $\Delta H_{mix}/H_0$.

ΔH_{mix} is concave upwards which is similar to a parabolic curve. Obviously, when the content of Ni is 50 at. pct, the mixing enthalpy reaches a minimum value − 12.57 kJ·mol^{-1}. The ratio of ΔH_{mix} and H_0 describes the degree of deviation from the ideal solution, and is shown in Figure 4(d). The profile of $\Delta H_{mix}/H_0$ is opposite to the profile of ΔH_{mix} and is concave downwards. It indicates that the maximum deviation from the ideal solution is 3.45 pct when the content of Ni is 50 at. pct.

The deviation between the actual alloy and ideal solution is related to the interaction of atoms. If the atomic interaction is repulsive force, a positive deviation will be observed which corresponds to positive excessive volume and mixing enthalpy. The positive mixing enthalpy implies phase separation will occur during alloying, *i.e.*, monotectic alloy systems such as Fe-Cu,[51] Ni-Ag[52] and Co-Ag[53] binary alloys. On the contrary, when the atomic interaction is attractive effect, a negative deviation will occur during alloying, as shown in Figure 4(c) and (d). Usually, there is a negative mixing enthalpy for miscible systems. According to Figure 4(c) and (d), it indicates that the Ni-Fe-Co ternary alloy is a miscible system and the atomic interaction is attractive force between the Ni and Fe/Co atoms.

B. *Liquid Structure of Ni-Fe-Co Alloys*

In order to investigate the microscopic mechanism that leads the change of thermodynamic properties, the pair distribution functions and static structure factors were calculated according to the atomic arrangement. Although the structural properties can be measured *via* the neutron-scattering[21,44] or X-ray diffraction[54,55] experiments, only the structural properties of pure Ni was reported for $Ni_{2x}Fe_{50-x}Co_{50-x}$ alloys. Figure 5(a) and (b) present the $g(r)$ and $S(q)$ of liquid Ni, it can be seen that the simulated results agree well with the experimental data of Vahvaselkä[56] and Waseda *et al.*.[57] Although the present nearest neighbor height of $g(r)$ is slightly bigger than the reported experimental values, the high-order neighbor is in good agreement with the measurement data of Vahvaselkä[56] by X-ray diffraction. Furthermore, the simulated profile of the $S(q)$ almost completely coincides with the experimental data of Vahvaselkä,[56] and both of the nearest neighbor distance of the $S(q)$ is 3.04 Å^{-1}, as shown in Figure 5(b). In the experiments, the $S(q)$ can be directly obtained from the diffraction data, and the $g(r)$ is calculated from the structure factor by Fourier transformation. Usually, the range of q of the $S(q)$ is smaller than 10 Å in the experimental data, therefore, the difference of the nearest neighbor height may be due to a small

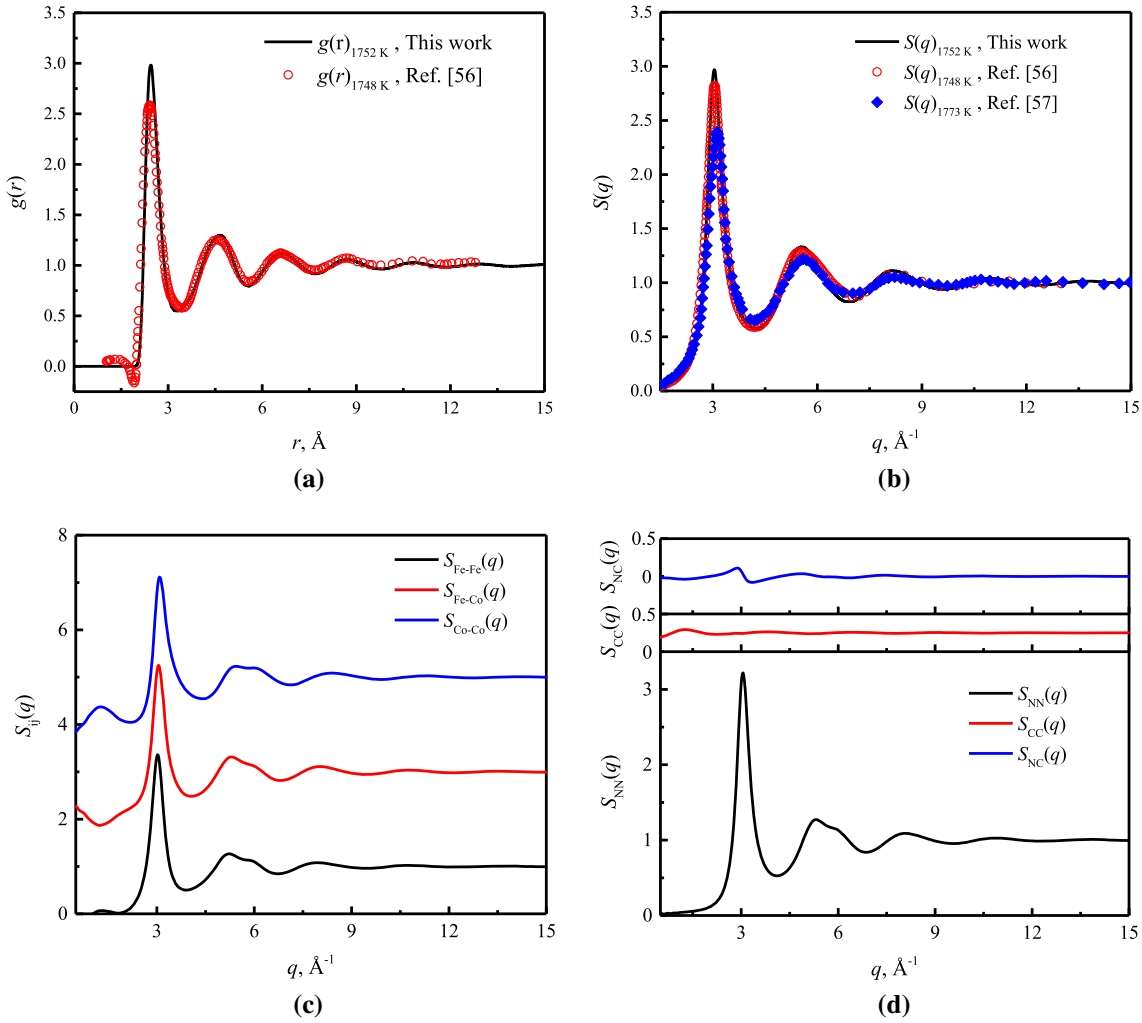

Fig. 5—MD simulation of liquid structure: (*a*) Pair distribution functions of liquid Ni at 1752 K; (*b*) Static structure factor of liquid Ni at 1752 K; (*c*) Partial static structure factors of liquid $Fe_{50}Co_{50}$ alloy at 1700 K; (*d*) Bhatia–Thornton partial structure factors of $Fe_{50}Co_{50}$ alloy at 1700 K.

measurement range. Waseda and Ohtani[57] have measured the structure factor of liquid Ni at 1773 K which is shown in Figure 5(b), and it can be seen that the amplitude of $S(q)$ is smaller than the measurement data by Vahvaselkä[56] and simulation value. It is well known that the amplitude of $S(q)$ will increase with the decrease of temperature. As a result of high temperature, there is a difference in amplitude of structure factor between the experiments and simulation.

The structural information of liquid $Fe_{50}Co_{50}$ alloy at 1700 K are illustrated in Figures 5(c) and (d). The Faber–Ziman partial static structure factors in Figure 5(c) show that there is a similar intensity of the peaks between the partial structure factors, and a shoulder appears on the right side of secondary neighbor of the $S_{ij}(q)$. Usually, the shoulder of the secondary neighbor is related to the icosahedral short-range order. Therefore, there are icosahedral structures in the undercooled liquid $Fe_{50}Co_{50}$ alloy. A pre-peak is displayed in the partial static structure factor of Co-Co, which indicates a medium-range order of Co-Co distribution. To investigate the topological and chemical short-range order of binary $Fe_{50}Co_{50}$ alloy, the Bhatia–Thornton static structure factors were calculated based on Eqs. [9] through [11] and illustrated in Figure 5(d). It can be seen that the amplitude of $S_{CC}(q)$ is very small and the value of $S_{CC}(q)$ is close to a constant 0.25 with the increase of the wave vector q. This result indicates that both Fe and Co atoms are uniformly mixed and there is not chemical short-range order in the liquid $Fe_{50}Co_{50}$ alloy. A small amplitude of $S_{NC}(q)$ suggests that the radius of Fe atom is close to Co atom and the structural properties of $Fe_{50}Co_{50}$ can be described by number-number partial static structure factor. The valley at $q = 1.25$ Å^{-1} of $S_{Fe\text{-}Co}(q)$ offsets the pre-peak of $S_{Co\text{-}Co}(q)$ and leads to smooth increasing of $S_{NN}(q)$ at corresponding location. The Bhatia–Thornton static structure factors show that the liquid $Fe_{50}Co_{50}$ alloy can be regarded as ideal solution. Brillo *et al.*[17] have measured the densities of Fe_xCo_{1-x} alloys using EML technique and proved the Fe-Co binary alloy can be described by an ideal solution model. Furthermore, Lee *et al.*[6] have reported the density of liquid Fe-Co binary alloy *via* ESL and indicated that the Fe-Co alloy almost like an ideal

solution. The simulated structural properties of pure Ni and $Fe_{50}Co_{50}$ alloy are in good agreement with the experimental data, and the agreement gives a confidence to further investigate the structural properties of $Ni_{2x}Fe_{50-x}Co_{50-x}$ alloys using this 2NN MEAM potential.

The partial pair distribution functions were calculated according to the atomic arrangement and shown in Figures 6(a) through (h). To clearly display the change of nearest and secondary neighbor, the magnified figures of the nearest and secondary neighbor are inserted in Figures 6(a) through (h), respectively. Figure 6(a) shows the total pair distribution functions of $Ni_{2x}Fe_{50-x}Co_{50-x}$ alloys at 1700 K, it can be seen that the height of nearest neighbor ($g(r_1)$) and the secondary neighbor distance (r_2) increase with the increase of Ni content, and the nearest neighbor distance (r_1) and the height of secondary neighbor ($g(r_2)$) slightly decreases with the Ni content. The more information of $g_{Total}(r_1)$, $g_{Total}(r_2)$, r_1 and r_2 are illustrated in Figure 6(i). A significant increase of $g_{Total}(r_1)$ indicates an increase of local atomic number density, corresponding with the enhancement of density. The partial pair distribution functions of Ni-Fe, Fe-Fe, Fe-Co and Co-Co show a similar trend vary with Ni content, as shown in Figures 6(c), (e) through (g). It can be found that the $g_{ij}(r_1)$ of Ni-Fe, Fe-Fe, Fe-Co and Co-Co decrease with the increase of Ni content, moreover, the nearest neighbor distance increases with the Ni content, the $g_{ij}(r_2)$ and r_2 of Fe-Co and Co-Co significant increase with the Ni content. On the contrary, the intensity and distance of secondary peak of Ni-Fe and Fe-Fe hardly

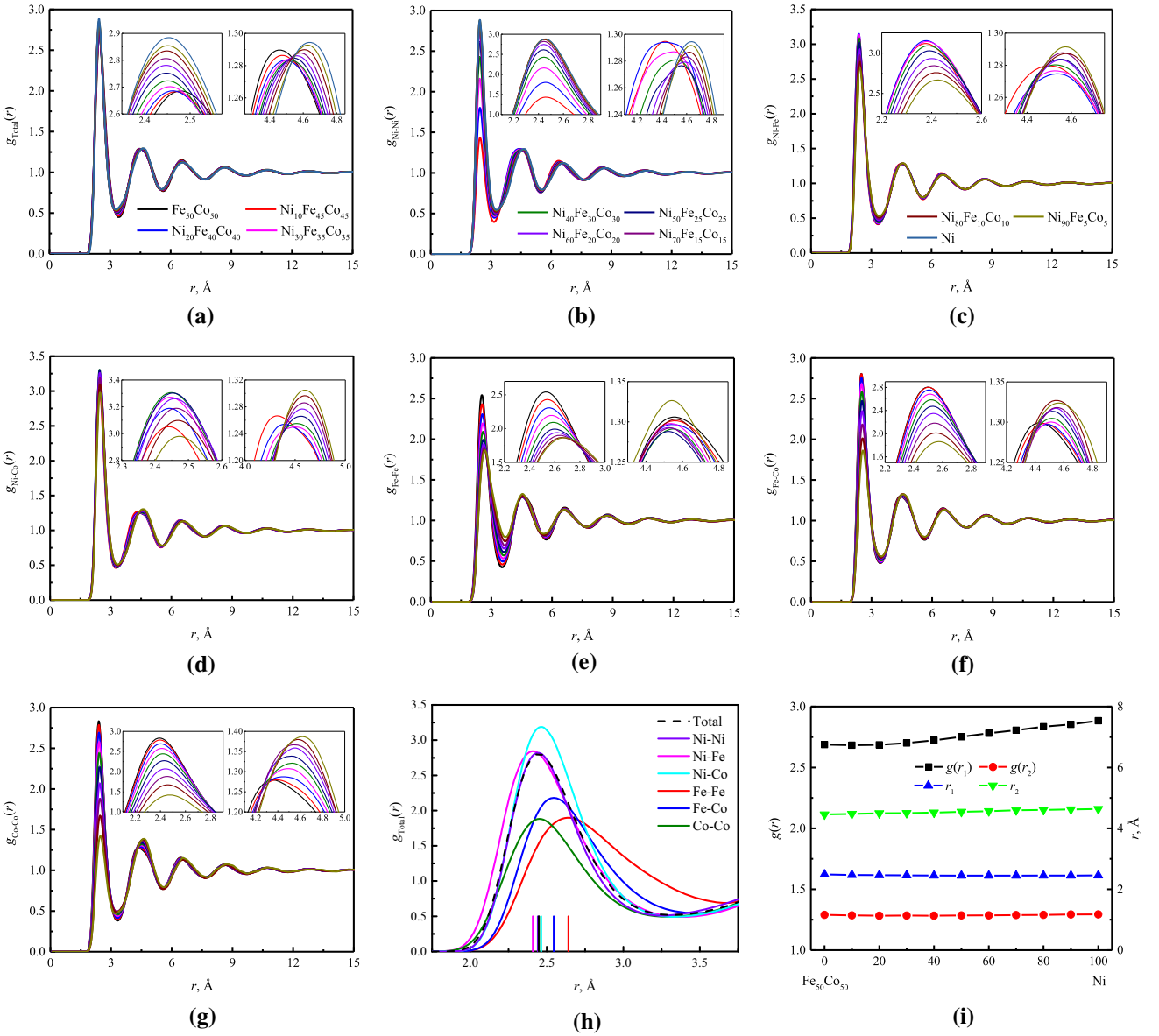

Fig. 6—Pair distribution functions of liquid $Ni_{2x}Fe_{50-x}Co_{50-x}$ alloys at 1700 K: (*a*) Total pair distribution functions; (*b*) through (*g*) Ni-Ni, Ni-Fe, Ni-Co, Fe-Fe, Fe-Co and Co-Co partial pair distribution functions, respectively; (*h*) Enlarged view of the first peaks of $Ni_{70}Fe_{15}Co_{15}$ alloy; (*i*) The first peak value and position of total pair distribution functions *vs.* Ni content.

change with increasing Ni content. The $g_{\text{Ni-Co}}(r_1)$ first increase and then decrease as the content of Ni increases, and the r_1 slightly increases with Ni content. When the Ni atoms are added in Ni-Fe-Co alloys, they will replace the Fe/Co atoms. Therefore, with the increase of Ni content, the $g_{\text{Ni-Co}}(r_1)$ will enhancement. However, when the content of Ni is larger than a certain value, the Ni atoms dominate the local structure of liquid Ni-Fe-Co alloys. Then, the $g_{\text{Ni-Co}}(r_1)$ will decrease with the increase of Ni content. Moreover, the intensity of the nearest neighbor of $g_{\text{Ni-Ni}}(r)$ increases with the enhancement of Ni content, and the r_1 of $g_{\text{Ni-Ni}}(r)$ slightly decreases with the Ni content. The change of secondary peak height and the distance of $g_{\text{Ni-Ni}}(r)$ and $g_{\text{Ni-Co}}(r)$ are similar with total pair distribution function. This indicates that the short-range structure of liquid $Ni_{2x}Fe_{50-x}Co_{50-x}$ alloys is determined by the Ni-Ni and Ni-Co interaction. It can be also found that the intensities of $g_{\text{Ni-Fe}}(r_1)$ and $g_{\text{Ni-Co}}(r_1)$ are larger than the other partial pair distribution functions, which indicates that Ni atoms are easily bond with Fe and Co atoms in the liquid $Ni_{2x}Fe_{50-x}Co_{50-x}$ ternary alloys. The nearest neighbor distance of $g_{ij}(r)$ is consistent with the length of chemical bond between i and j atoms. On the other hand, the bond length can be calculated by using Gold-Schmidt radius of Fe (r_{Fe} = 1.28 Å), Co (r_{Co} = 1.25 Å) and Ni (r_{Ni} = 1.25 Å) elements.[58] According to the Figures 6(b) through (g), it can be seen that the r_1 of Ni-Ni, Ni-Fe, Ni-Co and Co-Co is smaller than the corresponding bond length, and the nearest neighbor distance of $g_{\text{Fe-Fe}}(r)$ and $g_{\text{Fe-Co}}(r)$ is first smaller and then larger than the bond length with the increase of Ni content. It indicates that the attractive interactive exists in Ni-Ni, Ni-Fe, Ni-Co and Co-Co bond, and the interactive of Fe-Fe and Fe-Co bond change from attractive to repulsive force with increasing Ni content.

In order to investigate the relationship between the $g_{\text{Total}}(r)$ and $g_{ij}(r)$, the nearest neighbor of partial pair distribution functions and the first peak position of liquid $Ni_{70}Fe_{15}Co_{15}$ alloy at 1700 K are illustrated in Figure 6(h). It can be found that the nearest neighbor distance of $g_{\text{Ni-Fe}}(r)$ is smaller than the r_1 of $g_{\text{Total}}(r)$, the r_1 of $g_{\text{Ni-Ni}}(r)$, $g_{\text{Ni-Co}}(r)$ and $g_{\text{Co-Co}}(r)$ approximates the nearest neighbor distance of $g_{\text{Total}}(r)$, and the first peak position of $g_{\text{Fe-Fe}}(r)$ and $g_{\text{Fe-Co}}(r)$ is larger than the r_1 of $g_{\text{Total}}(r)$. This indicates that there are a short length of Ni-Fe bond, and long length of Fe-Fe and Fe-Co bonds in liquid $Ni_{70}Fe_{15}Co_{15}$ alloy. Further, it suggests that the Ni-Fe bond has a stronger attraction interactive than other bonds and the repulsive force of Fe-Fe bond is larger than Fe-Co bond in liquid $Ni_{70}Fe_{15}Co_{15}$ alloy.

The local atomic structure can be characterized by atomic packing, *i.e.*, the nearest neighbor coordination number *CN*. The CN_{ij} is the number of type atomic j in the nearest neighbor shell of central i atom and can be calculated by integrating the partial pair distribution function $g_{ij}(r)$ as follows[59]:

$$CN_{ij} = \int_0^{r_m} 4\pi r^2 \rho_j g_{ij}(r) \mathrm{d}r \qquad [15]$$

where r_m is the distance of first minimum of $g_{ij}(r)$, ρ_j the number density of type atomic j, r the distance.

The CN_{ij} of liquid $Ni_{2x}Fe_{50-x}Co_{50-x}$ alloys at 1700 K were calculated based on the corresponding partial pair distribution function and illustrated in histogram Figure 7. The partial coordination numbers of Ni-Ni, Fe-Ni and Co-Ni increase with increasing of Ni content. On the contrary, the total and other partial coordination numbers decrease as the content of Ni increases. Moreover, it can be found that the partial coordination numbers of Fe-Ni and Co-Ni are larger than the partial *CN* of Ni-Ni, which indicates that the Ni atoms are easier to bond with Fe and Co atoms than Ni atoms. Otherwise, the partial coordination numbers of Fe-Ni and Co-Ni are similar, and the partial *CN* of Ni-Fe is close to the Ni-Co. This suggests that Fe and Co have a similar characteristic to each other compared to Ni, *i.e.*, there are analogous interaction between Fe-Ni and Co-Ni, which is consistent with the assumption of Wang *et al.*[40] Although the total *CN* decreases with the increase of Ni content, the local atomic number density increases with the enhancement of Ni content due to r_m decreases with Ni content. The local atomic number densities ρ_{N1} of $Ni_{2x}Fe_{50-x}Co_{50-x}$ alloys were listed in Table I, it can be found that ρ_{N1} increases from 7.693 to 8.185 $\times 10^{-2}$ atoms·Å^{-1}. The improvement of local atomic number density leads to an increase of density with Ni content.

To further investigate the short-range and medium-range order structure, the Faber–Ziman partial static structure factor, $S_{ij}(q)$, was calculated based on Eq. [8]. The $S_{ij}(q)$ of different Ni content and wave vector were shown in Figure 8, and the corresponding enlarged figures of the nearest and secondary neighbor were inserted in Figures 8(a) through (f), respectively. Obviously, there is a pre-peak of $S_{\text{Ni-Ni}}(q)$, $S_{\text{Fe-Fe}}(q)$, $S_{\text{Fe-Co}}(q)$ and $S_{\text{Co-Co}}(q)$, and an shoulder on the secondary neighbor of $S_{\text{Ni-Fe}}(q)$, $S_{\text{Fe-Fe}}(q)$, $S_{\text{Fe-Co}}(q)$ and $S_{\text{Co-Co}}(q)$. It can be found that the pre-peaks of $S_{\text{Fe-Fe}}(q)$, $S_{\text{Fe-Co}}(q)$ and $S_{\text{Co-Co}}(q)$ increase with the enhancement of Ni content, on the contrary, the pre-peaks of $S_{\text{Ni-Ni}}(q)$ decrease with the Ni content. In particular, the positions of pre-peak of $S_{\text{Co-Co}}(q)$ increase with increasing of Ni content. The shoulders of $S_{\text{Fe-Ni}}(q)$, $S_{\text{Fe-Fe}}(q)$, $S_{\text{Fe-Co}}(q)$ and $S_{\text{Co-Co}}(q)$ gradually disappear as the Ni content increases. Usually, the pre-peak indicates medium-range order structure in liquid alloys, and the shoulder implies that icosahedral short-range order structure was contained in liquid alloys.[2,4,21,54,60] Therefore, there are medium-range and icosahedral short-range order structures in the liquid $Ni_{2x}Fe_{50-x}Co_{50-x}$ alloys. The medium-range order structures of Fe-Fe, Fe-Co and Co-Co bonds increase with the Ni content, and the sizes of Co-Co medium-range order structures decrease. On the other hand, the icosahedral short-range order structures of Ni-Fe, Fe-Fe, Fe-Co and Co-Co bonds disappear with the increase of Ni content. The valley before nearest-neighbor of $S_{\text{Ni-Fe}}(q)$ and $S_{\text{Ni-Co}}(q)$ neutralizes the pre-peak of other partial pair static structure factors and leads to gently increase of total static structure factor, namely

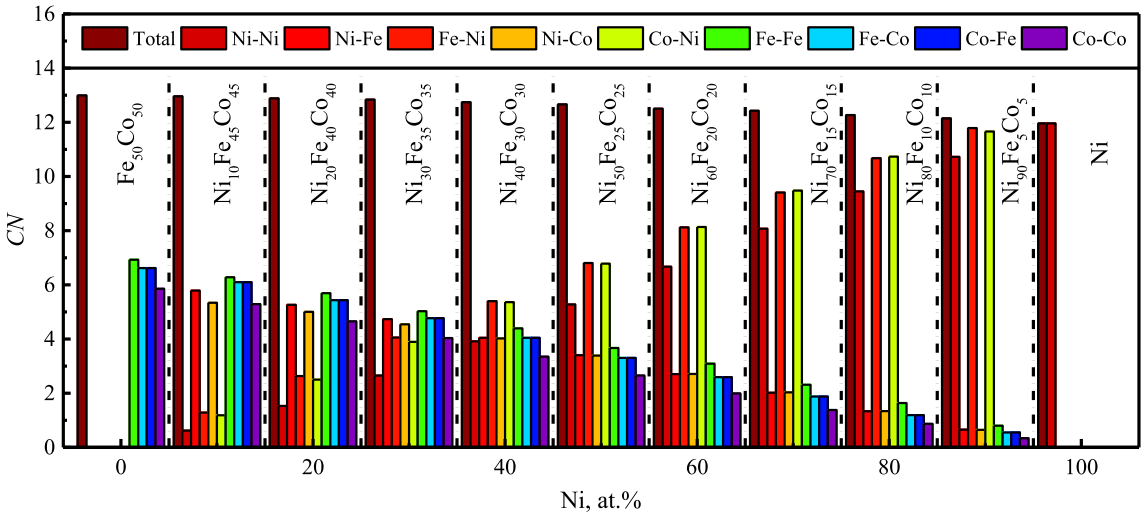

Fig. 7—Total and partial coordination number (*CN*) of $Ni_{2x}Fe_{50-x}Co_{50-x}$ alloys.

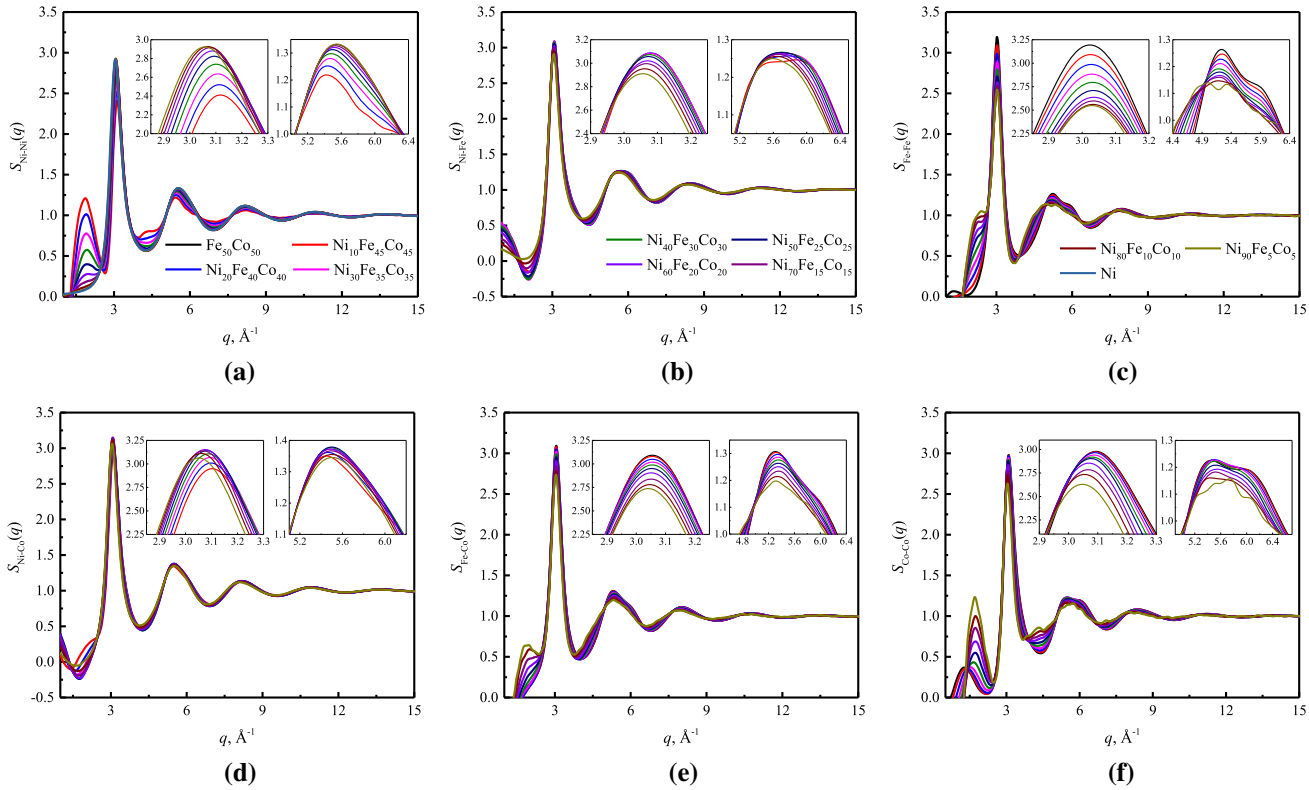

Fig. 8—Partial static structure factors of $Ni_{2x}Fe_{50-x}Co_{50-x}$ alloys at 1700 K: (*a*) Ni-Ni; (*b*) Ni-Fe; (*c*) Ni-Co; (*d*) Fe-Fe; (*e*) Fe-Co; (*f*) Co-Co.

$S_{NN}(q)$, at corresponding location, as shown in Figure 9(a).

The B–T static structure factors describe the topological and chemical short-range order structures of binary liquid alloys. The results of Figure 5(c) and (d) indicate that the $Fe_{50}Co_{50}$ alloy can be regarded as an ideal solution, which is consistent with the conclusion reported by Brillo *et al.*[17] and Lee *et al.*[6] Moreover, the partial coordination numbers suggest that Fe and Co have a similar characteristic to each other compared to Ni. Therefore, the ternary $Ni_{2x}Fe_{50-x}Co_{50-x}$ alloys can be approximated as the 'binary (FeCo)-Ni alloy', and the B–T static structure factors can be approximately calculated, as shown in Figure 9. It can be found that the nearest neighbor of $S_{NN}(q)$ slightly changes with the increase of Ni content. In order to clearly display the change of the secondary neighbor of $S_{NN}(q)$ with the Ni content, the enlarged figure of the second peaks of $S_{NN}(q)$ were shown in Figure 9(b). Obviously, the shoulder on the right hand

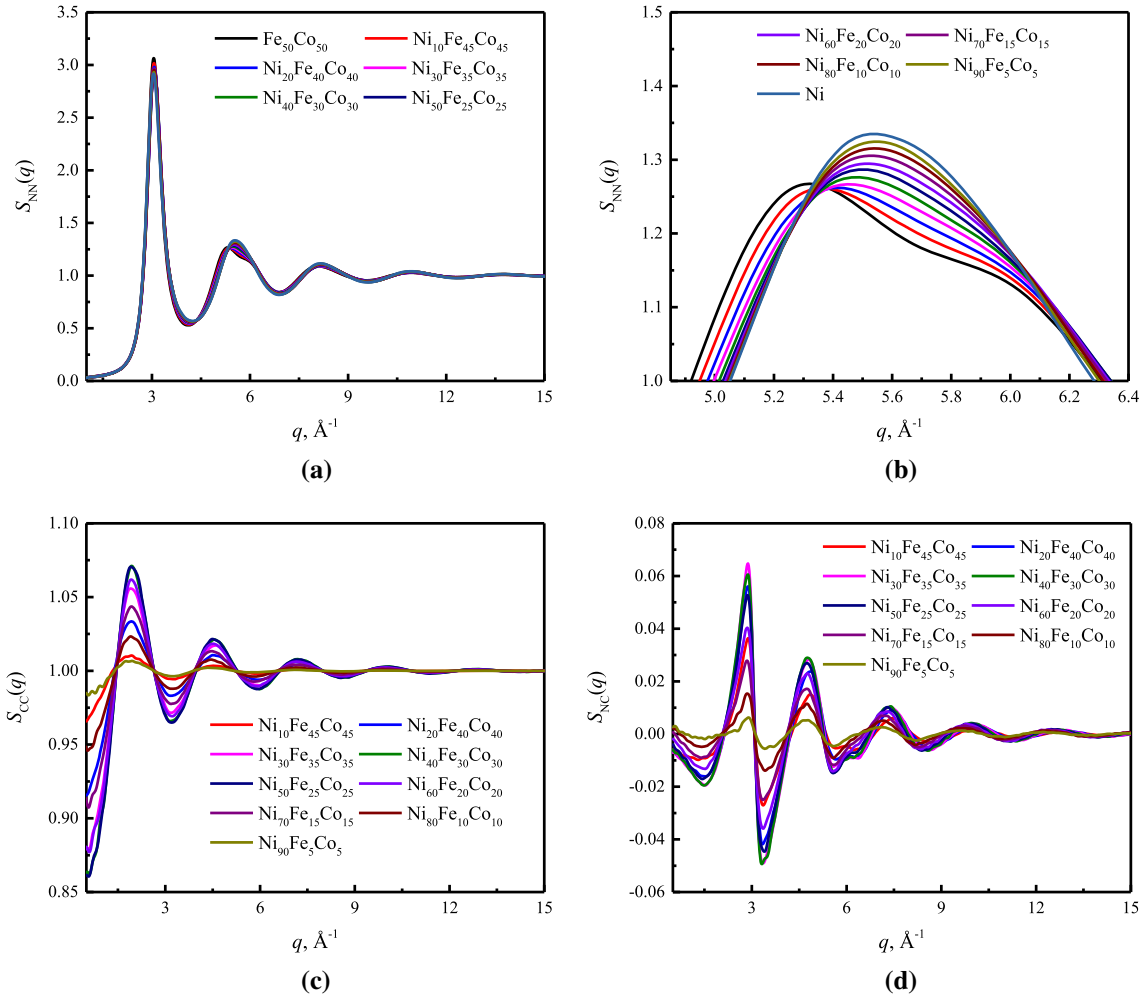

Fig. 9—Bhatia-Thornton number-number partial structure factors ($S_{NN}(q)$) of $Ni_{2x}Fe_{50-x}Co_{50-x}$ alloys at 1700 K: (*a*) S_{NN} (q) *vs.* wave vector q; (*b*) Enlarged view of the second peaks of $S_{NN}(q)$; (*c*) S_{CC} (q) *vs.* wave vector q; (*d*) S_{NC} (q) *vs.* wave vector q.

of the secondary neighbor gradually disappears with increasing Ni content, which suggests that the icosahedral short-range order structures disappear as the Ni content increases. The concentration-concentration static structure factors of $Ni_{2x}Fe_{50-x}Co_{50-x}$ alloys are presented in Figure 9(c). Obviously, the amplitude of $S_{CC}(q)$ first increases and then decreases with increasing Ni content, which suggests that the chemical short-range order structures increase to maximum at Ni content is 50 pct. Moreover, the $S_{CC}(q)$ of $Fe_5Co_5Ni_{90}$ alloy is almost close to a constant which means that this alloy can be regarded as ideal solution. Although the amplitude of $S_{NC}(q)$ changes with the Ni content, the values of number-concentration static structure factors are close to zero. The Gold–Schmidt radii of Fe (r_{Fe} = 1.28 Å), Co (r_{Co} = 1.25 Å) and Ni (r_{Ni} = 1.25 Å) elements are very close, so the $S_{NC}(q)$ of $Ni_{2x}Fe_{50-x}Co_{50-x}$ alloys is close to zero.

The Warren–Cowley parameter α_1 accurately describes the chemical short-range order.[61–63] Therefore, in order to quantitative estimate the relationship between the chemical short-range order and composition, the Warren–Cowley parameters of $Ni_{2x}Fe_{50-x}Co_{50-x}$ alloys were calculated as follows[61,62]:

$$\alpha_1 = 1 - \frac{CN_{ij}}{x_j(x_i CN_j + x_j CN_i)} \qquad [16]$$

with $CN_i = CN_{ii} + CN_{ij}$ (i,j = (FeCo), Ni)

where x_i is the concentration of type atomic i. A negative value declares that the different types of atoms tend to form the chemical bonds, *i.e.*, chemical short-range order. On the contrary, a positive value suggests that the same types of atoms tend to cluster, which implies a phase separation occurs in the liquid alloy. Moreover, the zero value means completely random distribution between the different types of atoms in alloy, which indicates the alloy is ideal solution.

Figure 10 presents the Warren–Cowley parameter α_1 as a function of composition. It can be seen that the α_1 first decreases to a minimum value and then increases to close to zero with increasing Ni content. A maximum chemical short-range order is observed when the Ni content is 40 pct. The decrease of α_1 corresponds to the increase of heterogeneous atomic bonds, which implies the decrease of mixing enthalpy, as shown in

Figure 4(d). The α_1 describes the heterogeneous atomic bonds of Ni-Fe and Ni-Co, and ignores the Fe-Co bond and other similar atomic bonds. However, the mixing enthalpy is a comprehensive effect about the different atoms. Therefore, there is a little difference of composition corresponding the minimum of α_1 and ΔH_{mix}.

C. *Solute Diffusion Dynamics of Liquid Ni-Fe-Co Alloys*

The diffusion coefficient describes the dynamic properties of alloys. In the MD simulation, the diffusion coefficient can be obtained by the slope of mean-square displacement (MSD)[25,59] *vs.* time according to the Einstein equation of diffusion:

$$D_j = \lim_{t\to\infty}\frac{1}{6t}\text{MSD}_j = \lim_{t\to\infty}\frac{1}{6t}\frac{1}{N_j}\sum_{i=1}^{N_j}\left|r_{i,j}(t) - r_{i,j}(0)\right|^2 \quad [17]$$

where N_j is the number of type atomic j, $r_{i,j}(t)$ the position of atom i at time t. Furthermore, the relationship between diffusion coefficient and temperature can be described by Arrhenius equation:

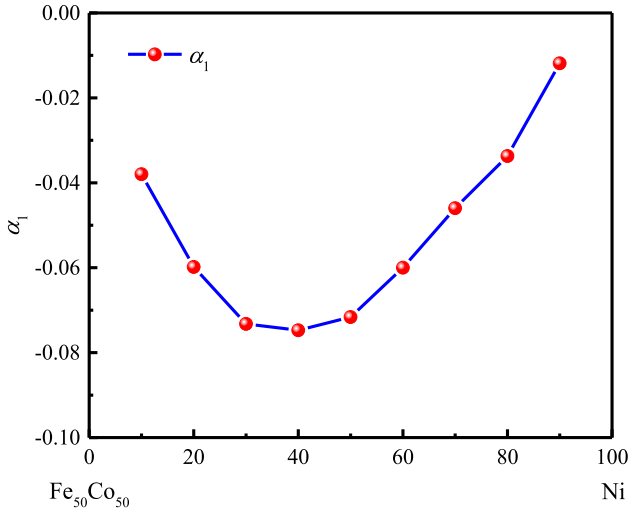

Fig. 10—The Warren–Cowley parameter of $Ni_{2x}Fe_{50-x}Co_{50-x}$ alloys.

$$D = D_0 \exp\left(-\frac{E_\alpha}{RT}\right) \quad [18]$$

where D_0 is pre-exponential factor, E_α the activation energy of diffusion, and R is ideal gas constant. The D_0 and E_α of liquid $Ni_{2x}Fe_{50-x}Co_{50-x}$ alloys are listed in Table II.

The diffusion coefficients, in a wide temperature range, of liquid $Ni_{2x}Fe_{50-x}Co_{50-x}$ alloys were obtained by monitoring the atomic motion. The more information of diffusion are listed in Table II. Figure 11(a) presents the mean-square displacement of liquid $Ni_{70}Fe_{15}Co_{15}$ alloy at 1700 K. It can be found that the MSD of Ni atom is the largest, Co atom has the smallest mean-square displacement, and the MSD of Fe atom is close to the total MSD. A larger MSD corresponds to a fast atomic migration, namely a larger diffusion coefficient. According to Eq. [17], the diffusion coefficients of liquid $Ni_{70}Fe_{15}Co_{15}$ alloy at different temperature can be calculated, as shown in Figure 11(b). The solid lines were obtained by fitting the diffusion coefficients based on Eq. [18]. To clearly display the relationship between the total and partial diffusion coefficients, the enlarged figure of diffusion coefficients is inserted in Figure 11(b). Obviously, the diffusion coefficient of Co atom is less than that of both Fe and Ni atoms, and the diffusion coefficient of Ni atom is slightly larger than that of Fe atom. In order to investigate the relationship between the diffusion behavior and composition, the diffusion coefficients of $Ni_{2x}Fe_{50-x}Co_{50-x}$ alloys at 1700 K were illustrated in Figure 11(c) and Table II. It can be seen that the total diffusion coefficient remains almost unchanged when the Ni content is less than 60 pct, and then the total diffusion coefficient increases as the Ni content increases. The density of liquid Ni is larger than the $Fe_{50}Co_{50}$ alloy at the same temperature. Therefore, the density of alloys will increase with the addition of Ni element. However, the increase of diffusion coefficient when the Ni content is larger than 60 pct, implies a significantly increase of volume, *i.e.*, the decrease of density, as show in Figure 4(a). Moreover, the trends of the partial diffusion coefficients of Ni and Fe atoms changing with composition are consistent with

Table II. The Calculated Solute Diffusion Parameters of Liquid $Ni_{2x}Fe_{50-x}Co_{50-x}$ Alloys

	Total			Fe			Co			Ni		
Compositions	D_0	E_α	D_T	D_0	E_α	D_T	D_0	E_α	D_T	D_0	E_α	D_T
Ni	110.04	53.44	2.51	–	–	–	–	–	–	110.04	53.44	2.51
$Ni_{90}Fe_5Co_5$	113.58	54.21	2.45	125.87	56.03	2.39	112.58	55.88	2.16	113.15	54.04	2.47
$Ni_{80}Fe_{10}Co_{10}$	109.01	54.26	2.35	112.19	54.73	2.34	115.54	56.86	2.07	107.94	53.91	2.38
$Ni_{70}Fe_{15}Co_{15}$	116.39	56.11	2.20	124.95	57.66	2.11	117.39	57.61	1.99	114.57	55.49	2.26
$Ni_{60}Fe_{20}Co_{20}$	116.11	56.62	2.11	112.28	56.13	2.12	117.24	57.79	1.97	117.12	56.43	2.16
$Ni_{50}Fe_{25}Co_{25}$	120.95	57.92	2.01	124.87	58.82	1.95	117.10	57.82	1.96	121.01	57.53	2.07
$Ni_{40}Fe_{30}Co_{30}$	119.12	57.75	2.00	118.85	58.24	1.93	121.91	58.34	1.97	117.44	56.98	2.08
$Ni_{30}Fe_{35}Co_{35}$	121.57	58.23	1.98	121.98	58.76	1.91	122.47	58.20	1.99	120.16	57.67	2.03
$Ni_{20}Fe_{40}Co_{40}$	117.61	57.57	2.00	118.44	58.11	1.94	116.60	57.16	2.04	118.15	57.34	2.04
$Ni_{10}Fe_{45}Co_{45}$	130.23	59.54	1.93	133.42	60.44	1.85	129.50	59.15	1.97	120.86	57.47	2.07
$Fe_{50}Co_{50}$	138.64	60.83	1.87	140.14	61.48	1.81	137.29	60.22	1.94	–	–	–

The units of D_0, E_α and D_T are 10^{-9} m^2/s, kJ/mol and 10^{-9} m^2/s, respectively.

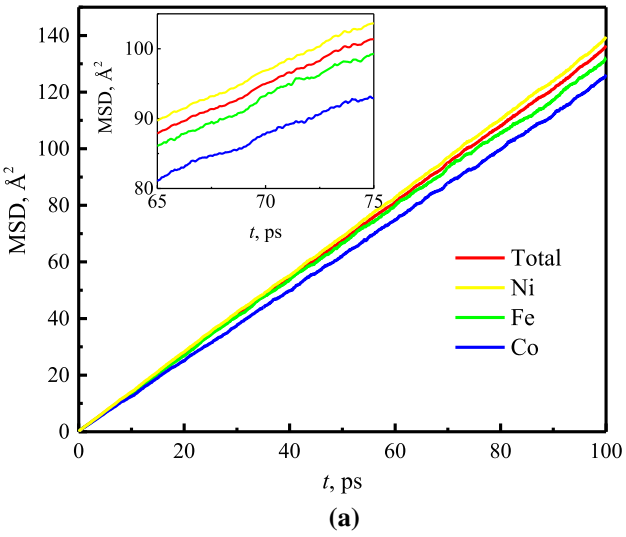

(a)

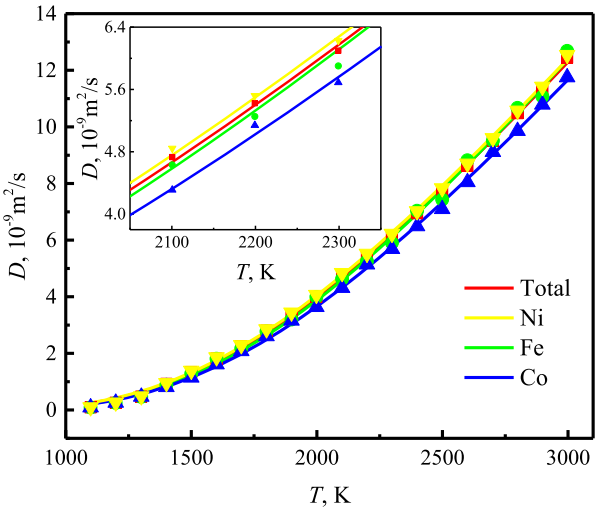

(b)

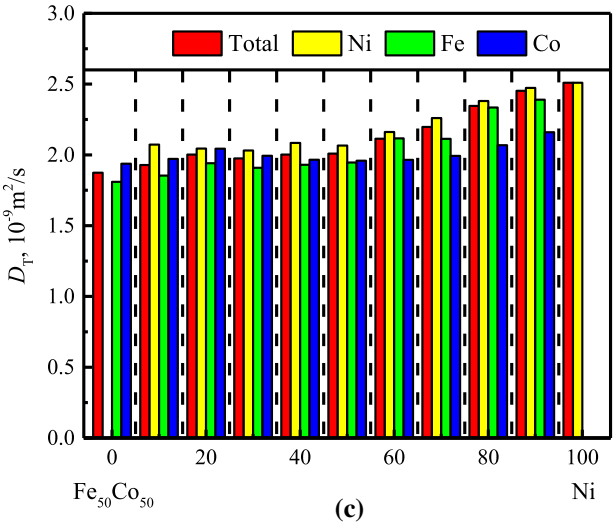

(c)

Fig. 11—Diffusion dynamics of $Ni_{2x}Fe_{50-x}Co_{50-x}$ alloys at 1700 K: (*a*) mean-square displacements of $Ni_{70}Fe_{15}Co_{15}$ alloy at 1700 K; (*b*) diffusion coefficients of $Ni_{70}Fe_{15}Co_{15}$ alloy at different temperature; (*c*) diffusion coefficients of $Ni_{2x}Fe_{50-x}Co_{50-x}$ alloys at 1700 K *vs*. Ni content.

the trend of the total diffusion coefficient. However, the diffusion coefficient of Co atom remains almost as a constant with the increase of Ni content. Therefore, the dynamic behavior of liquid $Ni_{2x}Fe_{50-x}Co_{50-x}$ alloys as a function of composition is determined by the diffusion of Ni and Fe atoms.

Usually, a large diffusion coefficient corresponds to a small activation energy of diffusion. According to Table II, it can be found that the total E_α decreases as the Ni content increases, which has an opposite trend to total diffusion coefficient with Ni content. A large total E_α indicates a high atomic packing in liquid alloys, namely large total *CN*. Therefore, the total *CN* decreases as the Ni content increases, which is consistent with the results in Figure 7.

IV. CONCLUSIONS

The structural, thermodynamic and dynamic properties of normal and metastable liquid $Ni_{2x}Fe_{50-x}Co_{50-x}$ alloys were systematically investigated by combining ESL experiments and MD simulations. Their composition dependence and mutual interaction were discussed in this work, respectively. The main conclusions are summarized as follows:

(1) The solidus and liquidus temperatures of ternary $Ni_{2x}Fe_{50-x}Co_{50-x}$ (x = 5, 10, 15, …,50) alloys were determined by the thermal analysis experiments, and the T_S and T_L decrease as the Ni content increases. The actual densities, in a wide temperature range, of liquid $Ni_{90}Fe_5Co_5$, $Ni_{80}Fe_{10}Co_{10}$, $Ni_{70}Fe_{15}Co_{15}$ and $Ni_{60}Fe_{20}Co_{20}$ alloys were obtained by ESL experiments with the consideration of the mass evaporation. The maximum undercoolings of liquid $Ni_{90}Fe_5Co_5$, $Ni_{80}Fe_{10}Co_{10}$, $Ni_{70}Fe_{15}Co_{15}$ and $Ni_{60}Fe_{20}Co_{20}$ alloys are 171 K, 189 K, 300 K and 312 K, respectively. The densities at liquidus temperatures increase from 7.690 to 7.868 g·cm^{-3} with the increase of the Ni content.

(2) The calculated densities of MD simulation are in good agreement with the experimental data, which confirms the accuracy of the thermodynamic properties and extends the temperature ranges. The thermal expansions of liquid alloys increase with the Ni content. The excess volume and mixing enthalpy of the $Ni_{2x}Fe_{50-x}Co_{50-x}$ alloys indicate that they are miscible alloy and the atomic interaction is attractive effect. Moreover, those alloys are farthest from the ideal solution when the Ni content is 50 pct.

(3) The B–T static structure factors of $Fe_{50}Co_{50}$ alloy indicate this alloy can be regarded as an ideal solution. The partial pair distribution functions and *CN* suggest that Fe and Co atoms easily bond with Ni atoms and have a similar characteristic to each other if compared with Ni atoms. The partial static structure factors show that there are icosahedral short-range and medium-range orders of Ni-Ni, Fe-Fe, Fe-Co and Co-Co bonds in the

liquid $Ni_{2x}Fe_{50-x}Co_{50-x}$ alloys. The B–T static structure factors of liquid $Ni_{2x}Fe_{50-x}Co_{50-x}$ alloys indicate the icosahedral short-range order gradually disappears as the Ni content increases and the chemical short-range order structures reach the maximum if the Ni content is 50 pct.

(4) The dynamic property reveals that the trend of the partial diffusion coefficients of Ni and Fe atoms change with composition are consistent with the trend of the total diffusion coefficient, and the partial diffusion coefficients of Co atoms remains almost a constant value. This suggests that the dynamic behavior of liquid $Ni_{2x}Fe_{50-x}Co_{50-x}$ alloys as a function of composition is determined by the diffusion of Fe and Ni atoms.

(5) With the increase of Ni content, a significant increase of $g_{\mathrm{Total}}(r_1)$ indicates an increase of local atomic number density, which corresponds to the enhancement of density. The decrease of total *CN* suggests the reduction of atomic packing, namely decrease of diffusion activation energy, which implies an increase of diffusion coefficients. An enhancement of chemical short-range order indicates the increase of heterogeneous atomic bonds, which implies the decrease of mixing enthalpy, *i.e.*, further deviation from the ideal solution. Moreover, an increase of diffusion coefficients reveals a reduction of atomic interaction, which suggests an enhancement of volume expansion.

ACKNOWLEDGMENTS

This work was supported by the National Natural Science Foundation of China (Grant Nos. 51734008, 52088101), the National Key R&D Program of China (Grant No. 2018YFB2001800) and the Shaanxi Key Industry China Program (Grant No. 2019ZDLGY05-10). We thank Dr. D. L. Geng and Dr. L. Wang for their help with the experiments. Furthermore, we are deeply grateful to Mr. M. X. Li and C. Liang for valuable discussion.

REFERENCE

1. M. Guerdane, F. Wendler, D. Danilov, H. Teichler and B. Nestler, *Phys. Rev. B* 2010, vol. 81, art. no. 224108.
2. H. L. Peng, T. Voigtmann, G. Kolland, H. Kobatake and J. Brillo, *Phys. Rev. B* 2015, vol. 92, art. no. 184201.
3. H. P. Wang, P. Lü, X. Cai, B. Zhai, J. F. Zhao and B. Wei, *Mater. Sci. Eng. A* 2020, vol. 772, art. no. 138660.
4. K. F. Kelton, G. W. Lee, A. K. Gangopadhyay, R. W. Hyers, T. J. Rathz, J. R. Rogers, M. B. Robinson and D. S. Robinson, *Phys. Rev. Lett.* 2003, vol. 90, art. no. 195504.
5. H. Cheng, Y. J. Lü and M. Chen, *J. Chem. Phys.* 2009, vol. 131, art. no. 044502.
6. J. Lee, J.E. Rodriguez, R.W. Hyers, and D.M. Matson: *Metall. Mater. Trans. B*, 2015, vol. 46B, pp. 2470–75.
7. P.-F. Paradis, T. Ishikawa, G.-W. Lee, D. Holland-Moritz, J. Brillo, W.-K. Rhim, and J.T. Okada: *Mater. Sci. Eng. R Rep.*, 2014, vol. 76, pp. 1–53.
8. L. Hu, S. J. Yang, L. Wang, W. Zhai and B. Wei, *Appl. Phys. Lett.* 2017, vol. 110, art. no. 164101.
9. Zheng Wang, Fan Yang, Andrea Bernasconi, Konrad Samwer and Andreas Meyer, *Phys. Rev. B* 2018, vol. 98, art. no. 024204.
10. J. Brillo and I. Egry: *Int. J. Thermophys.*, 2007, vol. 28, pp. 1004–16.
11. J. Brillo, I. Egry, and T. Matsushita: *Int. J. Thermophys.*, 2006, vol. 27, pp. 1778–91.
12. Sangho Jeon, Michael P. Sansoucie, Olga Shuleshova, Ivan Kaban and Douglas M. Matson, *J. Chem. Phys.* 2020, vol. 152, art. no. 094501.
13. H.P. Wang, C.H. Zheng, P.F. Zou, S.J. Yang, L. Hu, and B. Wei: *J. Mater. Sci. Technol.*, 2018, vol. 34, pp. 436–39.
14. A.K. Rai, H. Trpathy, R.N. Hajra, S. Raju, and S. Saroja: *J. Alloys Compd.*, 2017, vol. 698, pp. 442–50.
15. S.A. Uporov, V.A. Bykov, and D.A. Yagodin: *J. Alloys Compd.*, 2014, vol. 589, pp. 420–24.
16. R.C. Bradshaw, M.E. Warren, J.R. Rogers, T.J. Rathz, A.K. Gangopadhyay, K.F. Kelton, and R.W. Hyers: *Ann. N. Y. Acad. Sci.*, 2006, vol. 1077, pp. 63–74.
17. J. Brillo, I. Egry, and T. Matsushita: *Int. J. Mater. Res.*, 2006, vol. 97, pp. 1526–32.
18. Paul-Francois Paradis, Takehiko Ishikawa, Yuki Watanabe and Junpei Okada, *Adv. Opt. Technol.* 2011, vol. 2011, art. no. 454829.
19. Hidekazu. Kobatake and Juergen. Brillo: *J. Mater. Sci.*, 2013, vol. 48, pp. 4934–41.
20. Manabu. Watanabe, Masayoshi. Adachi, and Hiroyuki. Fukuyama: *J. Mater. Sci.*, 2016, vol. 51, pp. 3303–10.
21. D. Holland-Moritz, S. Stuber, H. Hartmann, T. Unruh, T. Hansen and A. Meyer, *Phys. Rev. B* 2009, vol. 79, art. no. 064204.
22. Caroline Desgranges and Jerome Delhornmelle, *Phys. Rev. Lett.* 2019, vol. 123, art. no. 195701.
23. G. W. Lee, A. K. Gangopadhyay, K. F. Kelton, R. W. Hyers, T. J. Rathz, J. R. Rogers and D. S. Robinson, *Phys. Rev. Lett.* 2004, vol. 93, art. no. 037802.
24. F. Demmel, L. Hennet, S. Brassamin, D. R. Neuville, J. Kozaily and M. M. Koza, *Phys. Rev. B* 2016, vol. 94, art. no. 014206.
25. L. Huang, C. Z. Wang and K. M. Ho, *Phys. Rev. B* 2011, vol. 83, art. no. 184103.
26. E. Sondermann, N. Jakse, K. Binder, A. Mielke, D. Heuskin, F. Kargl and A. Meyer, *Phys. Rev. B* 2019, vol. 99, art. no. 024204.
27. H. Li, G.H. Wang, J.J. Zhao, and X.F. Bian: *J. Chem. Phys.*, 2002, vol. 116, pp. 10809–15.
28. N. Jakse and A. Pasturel, *Phys. Rev. B* 2016, vol. 94, art. no. 224201.
29. B. Nowak, D. Holland-Moritz, F. Yang, Th Voigtmann, Z. Evenson, T. C. Hansen and A. Meyer, *Phys. Rev. B* 2017, vol. 96, art. no. 054201.
30. Joseph R. Vella, Mohan Chen, Frank H. Stillinger, Emily A. Carter, Pablo G. Debenedetti and Athanassios Z. Panagiotopoulos, *Phys. Rev. B* 2017, vol. 95, art. no. 064202.
31. S. Sinyova, L. Dreval, R. Starykh, and O. Novoghilova: *J. Phase Equilibria Diffus.*, 2019, vol. 40, pp. 583–87.
32. H. P. Wang, M. X. Li, P. F. Zou, X. Cai, L. Hu and B. Wei, *Phys. Rev. E* 2018, vol. 98, art. no. 063106.
33. P.F. Zou, H.P. Wang, S.J. Yang, L. Hu, and B. Wei: *Chem. Phys. Lett.*, 2017, vol. 681, pp. 101–4.
34. J. Lee and D.M. Matson: *Int. J. Thermophys.*, 2014, vol. 35, pp. 1697–704.
35. B.J. Lee and M.I. Baskes: *Phys. Rev. B*, 2000, vol. 62, pp. 8564–67.
36. B.J. Lee, W.S. Ko, H.K. Kim, and E.H. Kim: *Calphad*, 2010, vol. 34, pp. 510–22.
37. E. Asadi, M. A. Zaeem, S. Nouranian and M. I. Baskes, *Phys. Rev. B* 2015, vol. 91, art. no. 024105.
38. E. Lee, K. R. Lee, M. I. Baskes and B. J. Lee, *Phys. Rev. B* 2016, vol. 93, art. no. 144110.
39. E. Asadi, M.A. Zaeem, S. Nouranian, and M.I. Baskes: *Acta Mater.*, 2015, vol. 86, pp. 169–81.
40. H. P. Wang, J. F. Zhao, W. Liu and B. Wei, *J. Appl. Phys.* 2018, vol. 124, art. no. 215107.
41. Diana. Farkas and Alfredo. Caro: *J. Mater. Res.*, 2018, vol. 33, pp. 3218–25.
42. S. Plimpton: *J. Comput. Phys.*, 1995, vol. 117, pp. 1–19.
43. T.E. Faber and J.M. Ziman: *Philos. Mag.*, 1965, vol. 11, pp. 153–73.

44. M. L. Johnson, M. E. Blodgett, K. A. Lokshin, N. A. Mauro, J. Neuefeind, C. Pueblo, D. G. Quirinale, A. J. Vogt, T. Egami, A. I. Goldman and K. F. Kelton, *Phys. Rev. B* 2016, vol. 93, art. no. 054203.
45. A.B. Bhatia and D.E. Thornton: *Phys. Rev. B*, 1970, vol. 2, pp. 3004–12.
46. P.S. Salmon, R.A. Martin, P.E. Mason, and G.J. Cuello: *Nature*, 2005, vol. 435, pp. 75–78.
47. P. S. Salmon, A. C. Barnes, R. A. Martin and G. J. Cuello, *Phys. Rev. Lett*. 2006, vol. 96, art. no. 235502.
48. J. Brillo and I. Egry: *Int. J. Thermophys*., 2003, vol. 24, pp. 1155–70.
49. P.F. Zou, H.P. Wang, S.J. Yang, L. Hu, and B. Wei: *Metall. Mater. Trans. A*, 2018, vol. 49A, pp. 5488–96.
50. J. Brillo, T. Schumacher, and K. Kajikawa: *Metall. Mater. Trans. A*, 2019, vol. 50A, pp. 924–35.
51. F. Soisson and C. C. Fu, *Phys. Rev. B* 2007, vol. 76, art. no. 214102.
52. A. Rapallo, G. Rossi, R. Ferrando, A. Fortunelli, B. C. Curley, L. D. Lloyd, G. M. Tarbuck and R. L. Johnston, *J. Chem. Phys.* 2005, vol. 122, art. no. 194308.
53. Z. Kuntova, G. Rossi and R. Ferrando, *Phys. Rev. B* 2008, vol. 77, art. no. 205431.
54. G. W. Lee, A. K. Gangopadhyay, R. W. Hyers, T. J. Rathz, J. R. Rogers, D. S. Robinson, A. I. Goldman and K. F. Kelton, *Phys. Rev. B* 2008, vol. 77, art. no. 184102.
55. Y. Zhang, R. Ashcraft, M. I. Mendelev, C. Z. Wang and K. F. Kelton, *J. Chem. Phys*. 2016, vol. 145, art. no. 204505.
56. K.S. Vahvaselkä: *Phys. Scripta*, 1981, vol. 24, pp. 59–64.
57. Y. Waseda and M. Ohtani: *Phys. Status Solidi B*, 1974, vol. 62, pp. 535–56.
58. W.F. Gale and T.C. Totemeier: *Smithells Metals Reference Book*, 8th ed., Elsevier, Burlington, 2004.
59. H. Weber, M. Schumacher, P. Jovari, Y. Tsuchiya, W. Skrotzki, R. Mazzarello and I. Kaban, *Phys. Rev. B* 2017, vol. 96, art. no. 054204.
60. B. Nowak, D. Holland-Moritz, F. Yang, Th Voigtmann, T. Kordel, T. C. Hansen and A. Meyer, *Phys. Rev. Mater*. 2017, vol. 1, art. no. 025603.
61. J.M. Cowley: *Phys. Rev*., 1950, vol. 77, pp. 669–75.
62. N. Jakse and A. Pasturel, *Appl. Phys. Lett*. 2014, vol. 105, art. no. 131905.
63. L. Y. Tian, H. Levamaki, M. Kuisma, K. Kokko, A. Nagy and L. Vitos, *Phys. Rev. B* 2019, vol. 99, art. no. 064202.